Geometry optimisation of a Cerenkov detector for LUXE

Luca Hartman, École Polytechnique Fédérale de Lausanne, Switzerland

Supervisors: L. Helary, R. Jacobs, DESY-FTX

September 7, 2022

Abstract

LUXE is a proposed experiment to study the electron-photon interactions in a strong electromagnetic field. A particular challenge in this design is the high rate of electrons, up to 10^9 particles per collision. To succeed in measuring the interesting properties, multiple detectors compose the experimental setup, amongst which a box containing multiple Cerenkov. In this study, the layout of the straws has been optimised considering detection efficiency, energy distribution reconstruction accuracy and energy resolution. An energy distribution reconstruction method has been tested and was found to be satisfactory. Multiple layout approaches satisfying the requirements have been found. Critical parameters defining the layout have been highlighted in an general improved understanding of their effects on the measurements. A preliminary estimate of the energy resolution achievable with such a Cerenkov detector has been obtained.

Contents

1. Introduction

While quantum electrodynamics (QED) is well understood in weak electromagnetic fields, theory predicts multiple effects in stronger fields that have not been experimentally verified. LUXE is a proposed experiment which will study electron-photon and positron-photon interactions. The experiment consists of an electron beam and intense laser pulses. The Lorentz boosted electrons interacting with the photons reach sufficiently high coupling strength to become non-perturbative. The collisions in the interaction point produce electrons and positrons; they are separated using a magnetic field. In this study, only the electrons are considered. The electron detection system consists of a tracker, a scintillating screen with cameras and a Cerenkov detector. This detector is composed of multiple tubes (called straws) that use the Cerenkov effect to create photons. Photo detectors are then used to record the data. The goal is to precisely measure the energy distribution of the electrons produced in the event [2].
In order to obtain the best measurements possible, the precise geometry of the Cerenkov detector must be optimised. As the experiment is in its design phase, the study is done entirely using Geant4 simulations [1]. The optimisation considers the detector efficiency, the agreement between the reconstructed and true energy distributions, as well as the energy resolution. A feasible design that remains cost effective has been considered.
In this report, a brief introduction to the relevant theoretical background will be given. An explanation of the methodology used precedes the results and the discussion.

2. Theory

2.1. LUXE physics

The strength of the of the electromagnetic fields in the interaction point between the electrons and the photons at LUXE is large enough that the perturbative approach so successful at lower energies breaks down. While the energy scale at which this behaviour is expected is to be very high, the Lorentz boosted electrons from the beam can reach sufficiently large coupling strength. In particular, the physics of interest at LUXE are the non-linear Compton, the non-linear Breit-Wheeler and the non-linear trident effects. In order to quantify the strength of the laser field, the classical non-linearity parameter $\xi = m_e c^2 \epsilon_L / (\hbar \omega_L \epsilon_{CR})$ is introduced, where m_e is the electron mass, c the speed of light in vaccum, ϵ_L is the laser electric field magnitude and ω_L is the laser frequency. The Schwinger limit $\epsilon_{CR} = m_e^2 c^3 / (e\hbar)$ is the typical field magnitude in QED.
For further information about the physics in the LUXE experiment, see the Conceptual Design Report of the LUXE experiment [3].

2.2. Cerenkov effect

The Cerenkov effect is caused by charged particles in a dielectric medium when the particles move faster than the speed of light in the medium. In particular, the charged

particle disturbs the dipoles present in the medium. The speed at which the particle disturbs is too large for the dipoles to find a symmetric position. Therefore, the dipole field does not vanish and an electromagnetic radiation is produced. For a speed of light $c_n = c/n$, where c is the speed of light and n the diffraction coefficient of the medium, the condition is $v > c_n$. This is equivalent to $1/(\beta n) < 1$. In that case, a light cone with opening angle is produced; the opening angle θ is given by $\cos\theta = 1/(\beta n)$ [4].
The Frank-Tamm formula gives the number of photons N_γ produced by Cerenkov radiation per wavelength λ, as given in Equation 1

$$\frac{dN_\gamma}{d\lambda} = \frac{\epsilon(\lambda) q^2 l}{4\pi} \left(1 - \frac{c^2}{v^2 n^2(\lambda)}\right), \tag{1}$$

where α is the electric wavelength dependent permeability, l is the path length and $n(\lambda)$ the index of refraction of the medium [5].

2.3. LUXE experiment

The LUXE experiment consists of the electron beam (XFEL.EU beam), the laser pulse, the magnet and the detectors. The interaction between the electrons and the photons creates electrons and positrons; these are then separated by the magnet. Following the direction of the electron beam, the positrons are sent left, while the electrons are sent right. Since this study is entirely focused on the latter, only the right-hand part will be described. This part of the experiment is shown schematically on Figure 1. The electrons first hit the scintillating screen before entering the Cerenkov box. It is composed of multiple straws, ordered in layers. There is a gap between the electron beam (which goes straight down the middle) and the first (left-most) straw. A electron dump is placed behind the Cerenkov box.

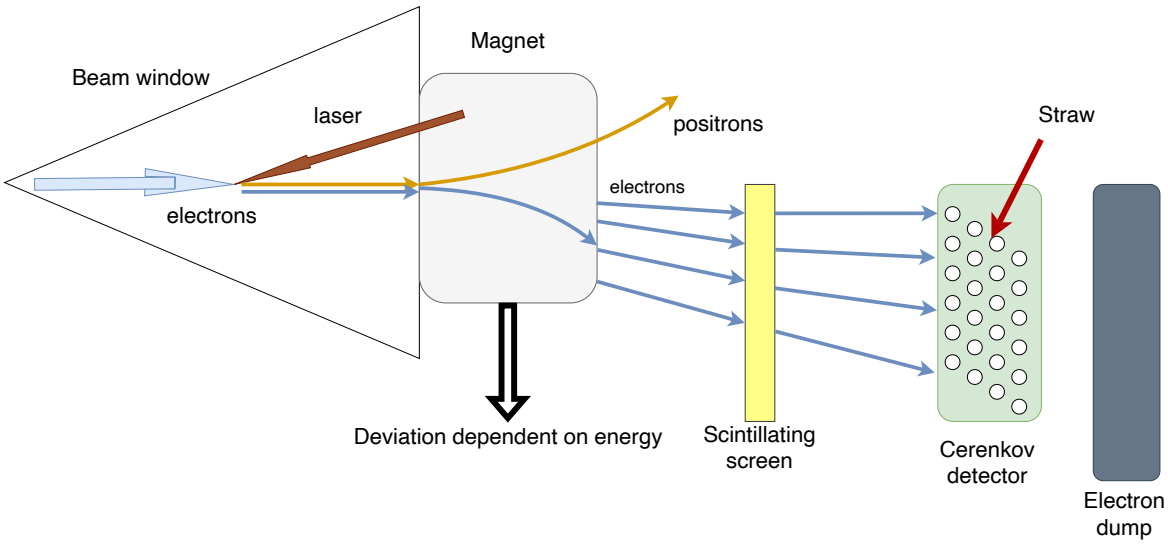

Figure 1: Schematic view of the LUXE experiment on the electron side.

Each straw is defined by its radius, its length, its position and its material. The photons created by the passage of the electron in the air bounces on the wall and reaches the top. At this position, a photo-multiplier is placed to record the data. This data is recorded individually for each straw by a commonly shared electronics board. Because of the electronic board, the straws can be densely packed along one direction, but not multiple. The electron energy required to detect an electron is of the order of 2 MeV. The material of the straw has not been fixed yet. Most of the layouts presented in this study are have been made using a multilayered straw containing (from innermost to exterior): graphite, aluminium, Kapton, polyurethane, Kapton, aluminium and graphite. Simple aluminium and steel straws are also considered.

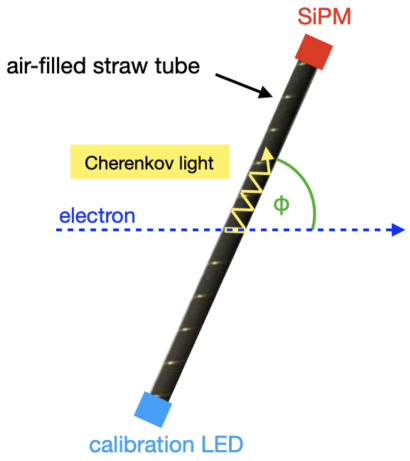

Figure 2: Illustration of a Cerenkov straw [2].

3. Methodology

This study has been executed entirely using tracks obtained from a reduced Geant4 simulation of the LUXE experiment containing the particle gun, simulating particles created at the the location of the electron-photon interaction point, the magnet and its vacuum chamber, the beam window, the scintillating screen, the cameras and the Cerenkov detector, as shown on Figure 1. In this report, the term "hit" has been used to describe any interaction between the electron and a solid object. The signal electron energy distribution has been obtained using the *Ptarmigan* generator [6].

3.1. Energy distribution reconstruction

Straw hit selection and front plane matching
The straw hits are considered if the energy is large enough for detection $E > 0.02$; this value is the Cerenkov threshold in air. Furthermore, two consecutive hits in the same straw are required. This represents an incoming and outgoing particle. To determine the energy of the electron, a virtual plane has been defined and implemented in the Geant4 simulation code. This plane is placed just in front of the Cerenkov box containing the straws, as can be seen on Figure 3. Every electron passing through this plane is considered to be of relevance if its energy is in the measurable range

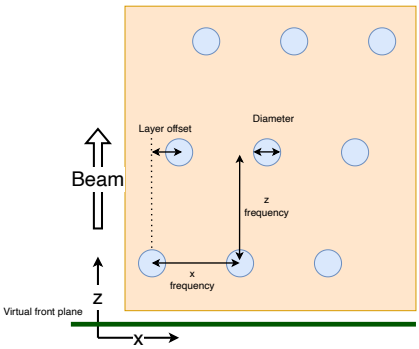

Figure 3: Sketch of the detector layout with the virtual front plane.

(0.02 GeV $< E <$ 16.5 GeV). The straw hits are
then associated to the front plane hits by extrapolating its position from the two straw hits. Only the x-coordinate and z-coordinate are extrapolated to the front plane position using the relation given in Equation 2

$$x_{\text{virtual plane}} = x_{\text{entry}} + (z_{\text{entry}} - z_{\text{virtual plane}}) \frac{x_{\text{exit}} - x_{\text{entry}}}{z_{\text{exit}} - z_{\text{entry}}}. \tag{2}$$

The front plane hit with the smallest distance $|x_{\text{exit}} - x_{\text{virtual plane}}$ is then selected as the associated front plane hit. This way, multiple electrons can be matched to the same front plane hit, which is necessary in case of electrons scattered inside the Cerenkov box. In the following steps, the energy of the electron E refers to its energy at the front plane.

Path length Once the experiment will start measurements, the actual information recorded will be the light produced inside each Cerenkov straw. Since simulating the light's behaviour is numerically expensive, a proxy variable has been selected. The total light yield in a Cerenkov straw is proportional to the total path length of all the electrons passing through. More precisely, the total path length $L = \sum_{\text{electron}} l_{\text{electron}}$ has been chosen as a proxy variable. It is defined as the sum of the relative path lengths l of each electron. For each electron of energy E, the path length $l_{i,E}$ in the straw number i is divided by the total length of the electron in the straws, as given by Equation 3,

$$l_{i,E} = \frac{|\vec{r}_{i,exit} - \vec{r}_{i,entry}|}{\sum_{j,E} |\vec{r}_{j,exit} - \vec{r}_{j,entry}|}, \tag{3}$$

where j is the index number of all the straws hit by this specific electron. The normalisation by the total path length is important in case the electron crosses multiple straws. The total path length of all electrons $L_{i,E}$ in the straw with identification number i at energy E is given in Equation 4

$$L_{i,E} = \sum_{\text{electrons}} l_{i,E} = \sum_{\text{electrons}} \frac{|\vec{r}_{i,exit} - \vec{r}_{i,entry}|}{\sum_{j,E} |\vec{r}_{j,exit} - \vec{r}_{j,entry}|}. \tag{4}$$

For examples, four cases are presented on Figure 4; the arbitrary values taken in the examples are not necessarily to scale. If an electron goes through only one straw along the diameter, this gives a contribution of 1; if it goes through one side, it gives a contribution of $L < 1$. If an electron goes through two straws on their respective diameters, it gives a contribution of $L = 1 + 1 = 2$; if it goes through two sides it gives for example $L = 0.6 + 0.55 = 1.15$.
The path length W_i in each straw identification number i is then defined by Equation 5

$$W_i = \sum_{\text{electrons}} |\vec{r}_{i,exit} - \vec{r}_{i,entry}|, \tag{5}$$

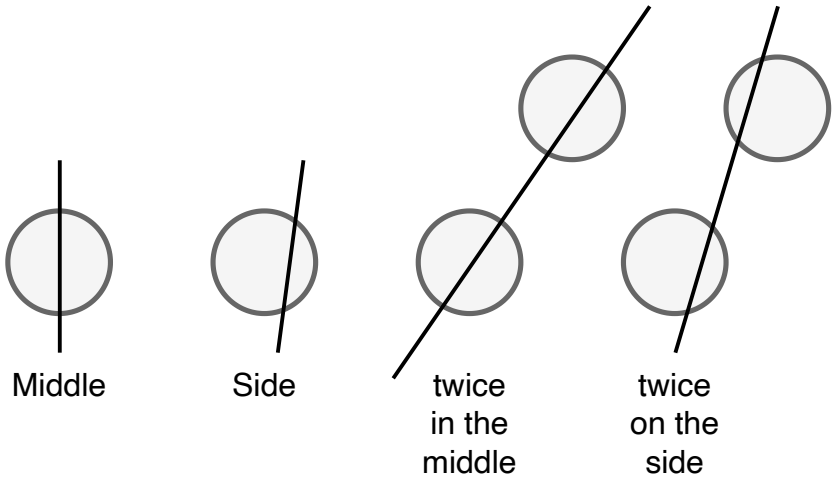

Figure 4: Schematic illustration of four different path length cases possible.

Flat sample and transfer matrix To have significant statistics across the whole energy range, 10 million electrons are simulated. The fact that it comes from a simulation allows for the definition of the matrix, as the trajectory is needed to compute the elements $L_{i,E}$. The electrons energies come from a flat energy distribution in order to avoid any bias.One can interpret $L_{i,E}$ as the elements of a matrix, called the transfer matrix, and W_i the elements of a vector. In that case, the transformation of the straw hit pattern recorded in the W_i to the energy distribution is simply a matrix-vector multiplication. The matrix is then normalised so that total sum over all energies is unitary for each straw is unitary

$$L_{i,E} \leftarrow \frac{L_{i,E}}{\sum_E L_{i,E}}.$$

Since the transfer matrix only has entries for successful matches between front plane hits and straw hits, the case of electrons missing all the straws needs to be taken into account separately. To achieve this, the energy distribution of the flat sample is reconstructed using the transfer matrix as if the distribution was unknown. A correction factor is computed for each energy so that the total number of reconstructed events $N_{E,\text{reco}}$ is equal to the true number of events $N_{E,\text{true}}$. This value is the acceptance A_E at energy E and is given by $A_E = N_{E,\text{true}}/N_{E,\text{reco}}$.

Signal sample Once the transfer matrix and the acceptance are derived, they are applied to the signal sample. This signal sample takes the original energy distribution obtained using the *Ptarmigan* generator for $\xi = 0.5$. The reconstructed number of events $N_{E,\text{reco}}$ the energy E is thus given by Equation 6

$$N_{E,\text{reco}} = \sum_i L_{i,E} W_i A_E. \tag{6}$$

Summary A graphical summary of the steps is shown on Figure 5. The flat sample selection and the signal sample selection can be done in parallel. Once the transfer matrix

and the energy acceptance are defined, they can be applied to the signal weighted path length distribution to obtain the signal energy distribution.

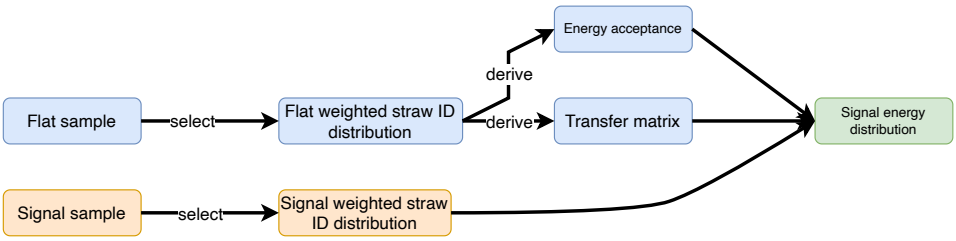

Figure 5: Diagram summarising the reconstruction method.

3.2. Energy resolution estimate

In order to estimate the energy resolution, mono-energetic electron samples have been simulated in the detector. Each sample contained 10′000 events, and the reconstructed energy distribution is obtained using the methodology discussed in Chapter 3.1. The energy distribution in the particle gun for $E = 9$ GeV and the energy distribution at the virtual front plane are shown overlayed on Figure 6.

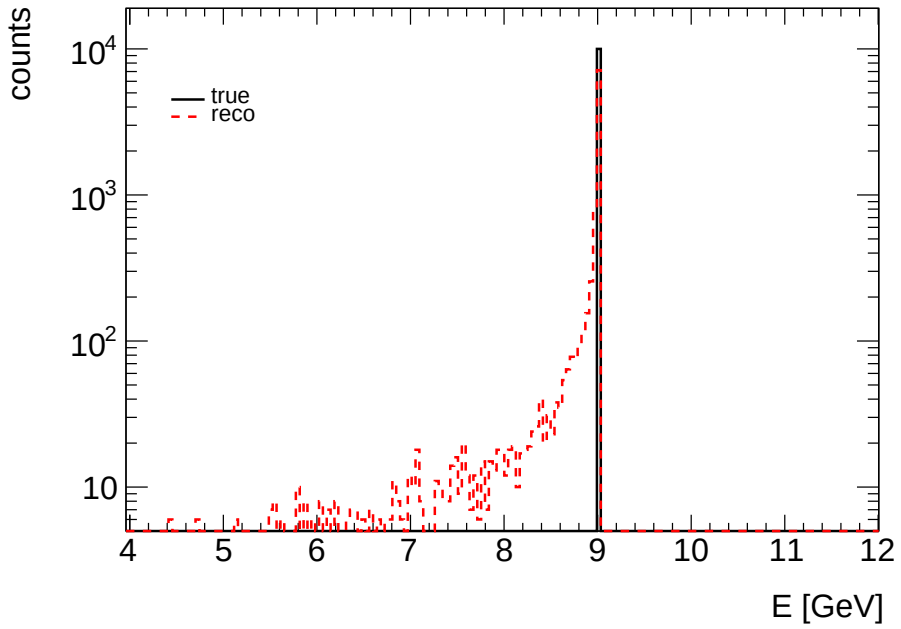

Figure 6: The energy distribution of the mono-energetic sample at the particle gun and the energy distribution of the mono-energetic sample at the virtual front plane.

A Crystal Ball function has been fitted to extract the energy resolution. It is effectively a Gaussian distribution with an power-law lower tail. In this study, the lower tails is

caused by the scattered electrons, which have lower energy. The function is defined by Equation 7 [7]

$$f(x;\alpha,n,\bar{x},\sigma) = N \cdot \begin{cases} \exp(-\frac{(x-\bar{x})^2}{2\sigma^2}, & \text{for } \frac{(x-\bar{x})}{\sigma} > -\alpha \\ A \cdot (B - \frac{(x-\bar{x})}{\sigma}, & \text{for } \frac{(x-\bar{x})}{\sigma} \leq -\alpha \end{cases} \tag{7}$$

where the constants are defined as follows

$$A = (\frac{n}{|\alpha|})^n \exp(-\frac{|\alpha|^2}{2}),$$

$$B = \frac{n}{|\alpha|} - |\alpha|,$$

$$N = \frac{1}{\sigma(C+D)},$$

$$C = \frac{n}{|\alpha|(n-1)} \exp(-\frac{|\alpha|^2}{2}),$$

$$D = \sqrt{\frac{\pi}{2}} \left(1 + \text{erf}(\frac{|\alpha|}{\sqrt{2}}\right).$$

In order to capture the energy dependance in the energy resolution, this simulation was repeated for energies ranging from 5 GeV to 15 GeV in steps of 1 GeV. Each mono-energetic sample has been fitted independently with the data around the peak (between $E-2$ GeV and $E+0.5$ GeV, where E is the energy of the particle gun). To compare the different layouts, the relative energy resolution σ_E/E has been used, with uncertainty $\Delta(\sigma_E/E)$ coming entirely by the uncertainty on $\Delta\sigma_E$ given by the fit.

3.3. Optimisation criteria

In order to optimise the geometry, specific criteria need to be defined. The ultimate condition for a good layout is a reconstructed energy distribution that perfectly follows the true distribution with little uncertainty. While it is important to consider this, it remains to vague to be fully effective. Therefore, additional criteria that are more narrowly defined have been used.

In order to measure precisely the electron energy distribution, the first criteria is having a high detection efficiency. This rate is defined a the number of events where at least one straw hit is matched to the front plane hit divided by the total number of events. This definition avoids the double counting occurring when simply dividing the number of straw hits by the number of virtual front plane hits; electron scattering in the Cerenkov box can compensate for the undetected "primary" electrons.

Furthermore, the energy acceptance should remain relatively flat for most of the energy range. This is important in order to have a clean reconstruction; large fluctuations impact negatively the smoothness of the reconstructed energy distribution.

For the energy resolution, general LUXE experiment considerations require a relative resolution of $\sigma_E/E < 2\%$.
Finally, the layout must be feasible and the cost should be reduced if possible. In particular, the number of straws should not be unnecessarily large, as each straw requires a photo-multiplier; photo-multipliers are a major cost driver.

4. Results

Different straw layouts have been evaluated during this study. The layouts are defined entirely by the set of parameters shown in Table 1. The diameter considered here is the inner diameter, i.e., the diameter of the Cerenkov volume. The x and z frequencies are defined as the distance between the centre of a straw to centre of the next one (along the x and z axes respectively). The offset is defined as the distance along the x axis between the centre of the left-most straw of a layer and the left-most straw of the next layer. For a graphical representation, see Figure 3. The results obtained for the layouts are shown in the following chapters.

	Channels	Layers	Diameter	x frequency	z frequency	Offset
Default	240	4	4.02 mm	16 mm	16 mm	4 mm
Single dense	100	1	4.02 mm	4.02 mm	16 mm	4 mm
Double dense	100	2	4.02 mm	4.02 mm	16 mm	4 mm
Varied sizes	$50, 50$	2	$4, 6$ mm	$4.1, 6.1$ mm	16 mm	4 mm
Heavily tilted	200	4	4.02 mm	8 mm	4.1 mm	4 mm

Table 1: Geometric parameters of the Cerenkov straw detector in its different layouts.

4.1. Default layout

The first studied geometry is that of a quadruple staggered layer. The relevant geometric parameters are given in Table 1. A part of the layout is shown in the xz plane on Figure 7a, where the straws continue on the positive x direction in a periodic manner and the axes are centred around the bottom left straw. The number of recorded straw hits per electron energy E is shown on Figure 7b. It was obtained using the flat sample. The efficiency of the Cerenkov detector as a function of the electron energy E is shown on Figure 8a, using the flat sample. The energy acceptance as a function of the energy E is presented on Figure 8b using a log vertical scale; it was obtained using the flat sample. It is clearly visible on Figure 7b that the large majority of electrons are detected. There is some events with more than four straw hits, which are most likely caused by scattered electrons. Nonetheless, some spots with no straw hit are visible are specific energies. This is confirmed by the efficiency plot, which shows drops at the same energies. The same drops are visible on the acceptance plot presented on Figure 8b. The most likely cause is electrons passing through the detector box without hitting any straw. While

the layout had been chosen so that it was without gap when looking from the front, the small angle of the electrons when entering the box allows for misses.
The reconstructed energy distribution and their Crystal Ball fit for multiple separate mono-energetic electron samples are shown on Figure 9. The energies of the samples cover the range from 5 GeV to 15 GeV in steps of 1 GeV. The reconstructed energy distributions of the mono-energetic samples are, as a first approximation, well modelled by Crystal Ball functions. These fits follow the lower tail well, but fails to properly reproduce the flat top of the main peak for higher energies. The main reason behind this is that the function aims to model a Gaussian distribution with a polynomial tail, which is not the behaviour seen in this study. The flat tops are caused by the straw thickness, which gives an almost uniform distribution for the energy range covered by the straw. Furthermore, the reconstruction method used in this work creates secondary peaks because of the drops in acceptance at some precise energies. These features are not reproduced by the Crystal Ball function. Secondary peaks above the main peak are also visible, with clear flat tops caused by the straw diameter.
The energy resolution σ_E/E estimated using the fits is shown as a function of the electron energy E on Figure 10. The energy resolution σ_E/E estimated using the fits have large relative variations from one energy to the other (at its worst, 100%). Furthermore, no clear trend is visible. Still, the energy resolution remains below the threshold value of 2%. The large variations at lower energies might be caused by the scattered electrons. Scattered electrons with high energies happen less often, meaning there is less noise in the data. This could explain why the expected rising tendency is only visible at high energies.
Finally, the true and reconstructed signal energy distributions are shown on Figure 11. The signal sample is obtained for $\xi = 0.5$. The energy distribution is well reconstructed using the method described in Chapter 3.1 for some parts, but pronounced inaccurate peaks are visible at energies where the acceptance drops. Therefore the efficiency criterion defined in Chapter 3.3 is useful. Also, the main peak visible in the true distribution is not properly reproduced in the reconstruction, this highlights the need for a good energy resolution, hence the 2% criterion. The reconstructed energy distribution for energies above 13 GeV is not a perfect match, as the true distribution is smoother.

4.2. Single dense layer layout

The second layout studied is that of a single layer of densely packed straws. The relevant geometric parameters are given in Table 1. A part of the layout is shown in the xz plane on Figure 12a, where the straws continue on the positive x direction in a periodic manner and the axes are centred around the bottom left straw. The number of recorded straw hits per electron energy E is shown on Figure 12b. It was obtained using the flat sample. The efficiency of the Cerenkov detector as a function of the electron energy E is shown on Figure 13a, using the flat sample. The energy acceptance as a function of the energy E is presented on Figure 13b using a vertical log scale; it was obtained using the flat sample.

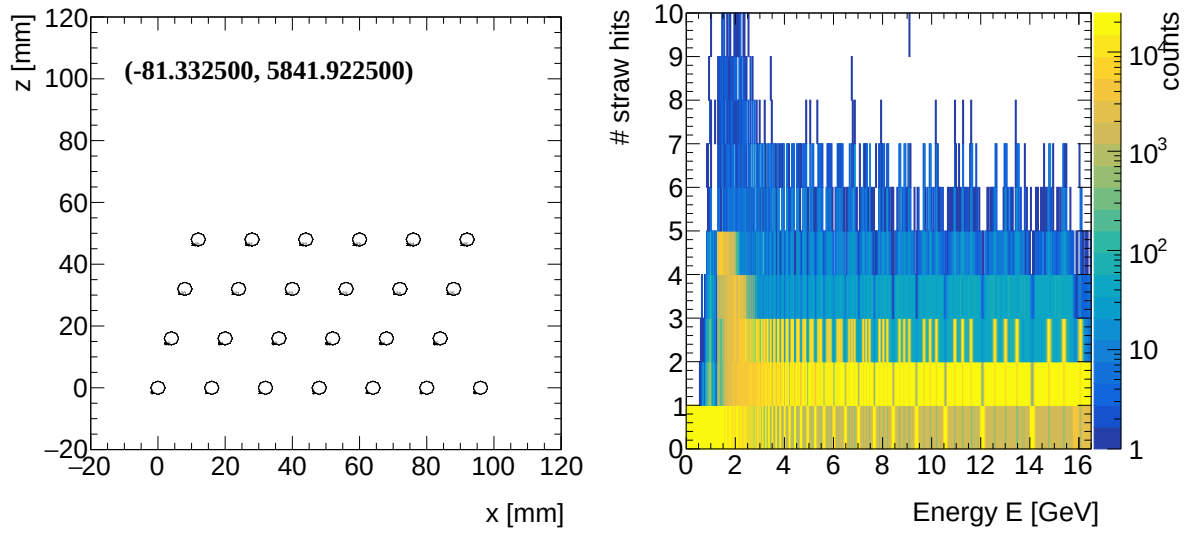

(a) (b)

Figure 7: Detector layout in the xz plane (a) and the number of straw hits per energy E (b) for the default layout. The axes are centred around the bottom left straw, which coordinates are written as a legend. The axes are the ones used in the LUXE Geant4 simulations.

Even though the number of straws has been reduced by more than half, the range of electron energy to which the detector is sensitive remains large. Effectively, all electrons with an energy larger than 3 GeV are detected. The drops are both smaller in width and in depth compared to the results obtained using the default layout. The limit of detectable energy is also clearly visible. The acceptance shows similar behaviour. These results suggest that electrons can not pass through the detector without hitting a straw, which is the expected behaviour based on the layout. The small drops are most likely caused by the electrons going through the straws in the thickness of the material, and thus not entering the air.

The reconstructed energy distribution and their Crystal Ball fit for multiple separate mono-energetic electron samples are shown on Figure 14. The energies of the samples cover the range from 5 GeV to 15 GeV in steps of 1 GeV. The reconstructed mono-energetic samples show a much smoother lower tail compared to the default layout. This is most likely caused by the fact that the efficiency drops are smaller. Nonetheless, fluctuations at energies higher than the true energy simulated are present. The Crystal Ball function is now more appropriate and the fit is visually a better approximation. Still, the main peak is flatter than the top of a Gaussian and therefore the energy resolution remains only an approximation.

The energy resolution σ_E/E estimated using the fits is shown as a function of the electron energy E on Figure 15. The relative energy resolution is showing the same large fluctuations as in the default layout. Yet, it still remains under the 2% threshold.

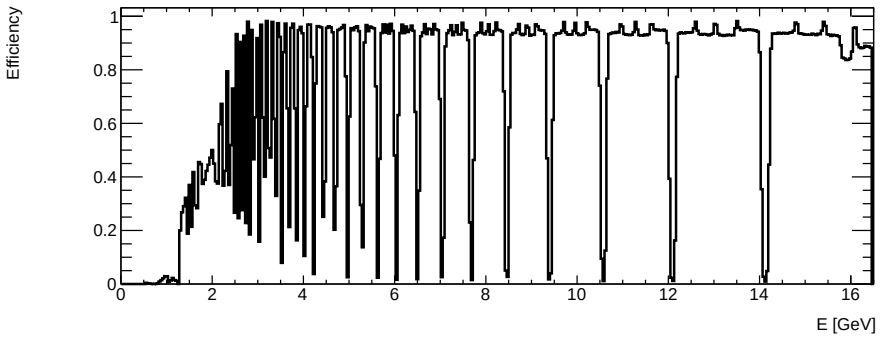

(a)

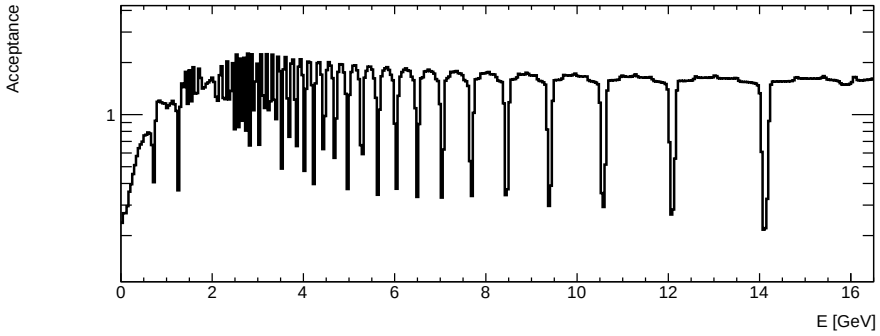

(b)

Figure 8: The detector efficiency (a) and the acceptance (b) as a function of the energy E for the default layout.

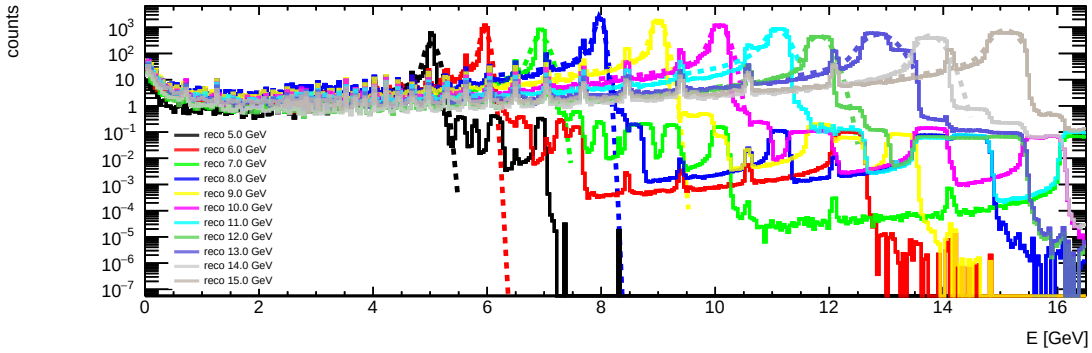

Figure 9: The reconstructed energy distribution for multiple mono-energetic electron samples at energies ranging from $E = 5$ GeV to $E = 15$ GeV with steps of 1 GeV (b). Those results were obtained for the default layout.

Finally, the true and reconstructed signal energy distributions are shown on Figure 16. The signal sample is obtained for $\xi = 0.5$. The reconstructed energy distribution matches very well the true energy distribution up to the Compton edge. The edge itself presents a

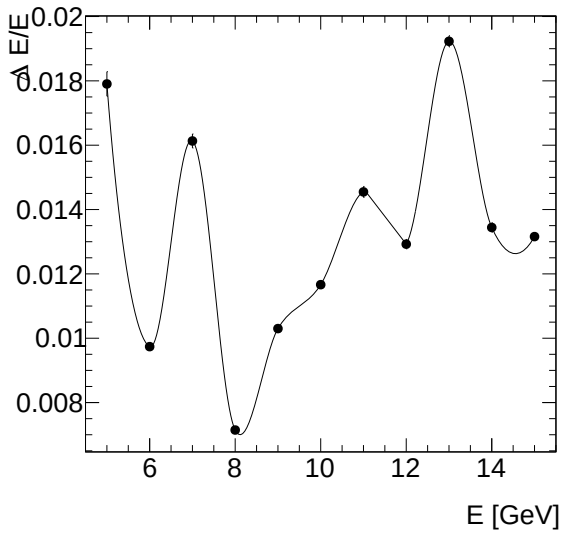

Figure 10: The energy resolution σ_E/E as a function of the energy E for the default layout.

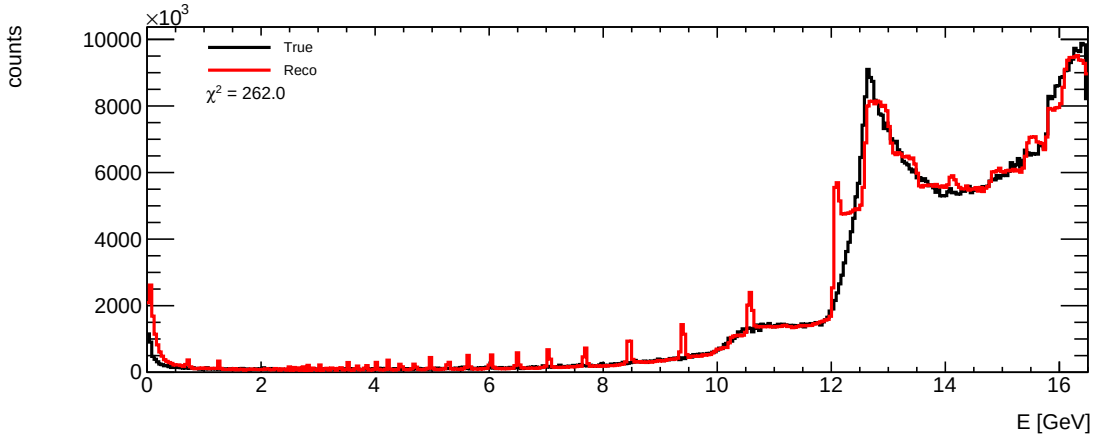

Figure 11: The true and reconstructed energy distributions obtained using the default layout.

bump in the reconstruction, but the position is still accurate. The reconstruction above the edge is wiggly, but follows the general tendency.

4.3. Double dense layer layout

The third layout studied is that of a double layer of densely packed straws. The relevant geometric parameters are given in Table 1. A part of the layout is shown in the xz plane on Figure 17a, where the straws continue on the positive x direction in a periodic manner and the axes are centred around the bottom left straw. The number of recorded

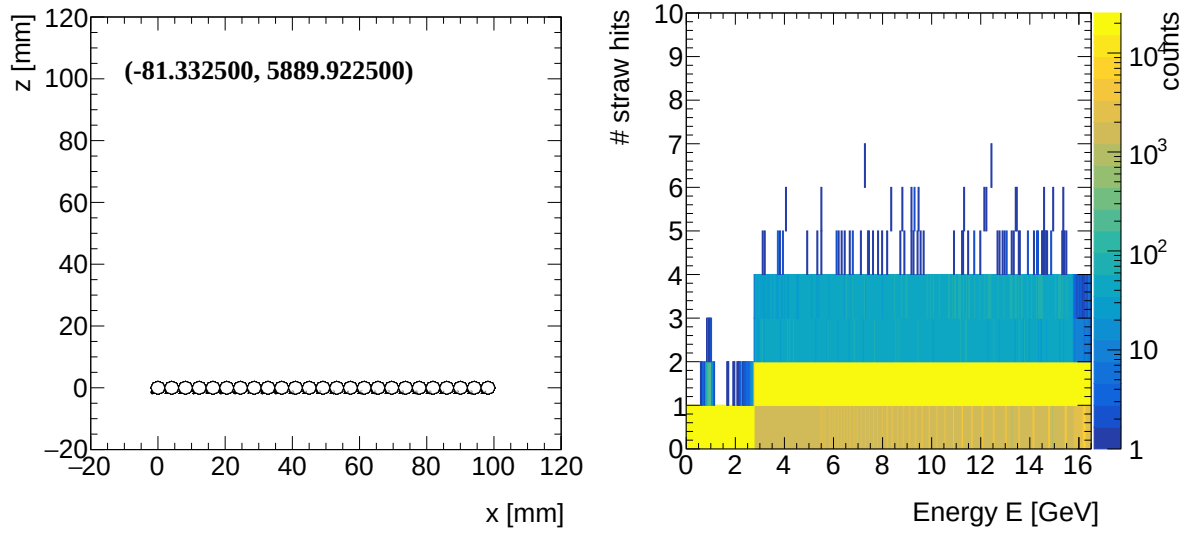

(a) (b)

Figure 12: Detector layout in the xz plane (a) and the number of straw hits per energy E (b) for the single dense layer layout. 4The axes are centred around the bottom left straw, which coordinates are written as a legend. The axes are the ones used in the LUXE Geant4 simulations.

straw hits per electron energy E is shown on Figure 17b. It was obtained using the flat sample.

For the double dense layer layout, Figure 17b shows clearly that most electrons are hitting two straws; most probably both layers. The lowest energy at which electrons are still detected is almost 5 GeV. As expected, this is higher than in the single dense layer layout, because the total number of straws is the same still. Therefore, the detector is shorter in the direction perpendicular to the beam. It is faintly visible that the highest energy electrons only hit one straw; they hit the left-most straw of the first layer. It is only a slightly lower energies that the electrons reach the left-most straw of the second layer.

The efficiency of the Cerenkov detector as a function of the electron energy E is shown on Figure 18a, using the flat sample. The energy acceptance as a function of the energy E is presented on Figure 18b using a log vertical scale; it was obtained using the flat sample. The behaviour described above can also be determined from the efficiency plot. Both the lower detection limit and the small efficiency drop off at high energies are visible. Nonetheless, the efficiency remains very high for most of the energy range. The acceptance remains perfectly flat.

The reconstructed energy distribution and their Crystal Ball fit for multiple separate mono-energetic electron samples are shown on Figure 19. The energies of the samples cover the range from 5 GeV to 15 GeV in steps of 1 GeV. The energy resolution σ_E/E estimated using the fits is shown as a function of the electron energy E on Figure 20.

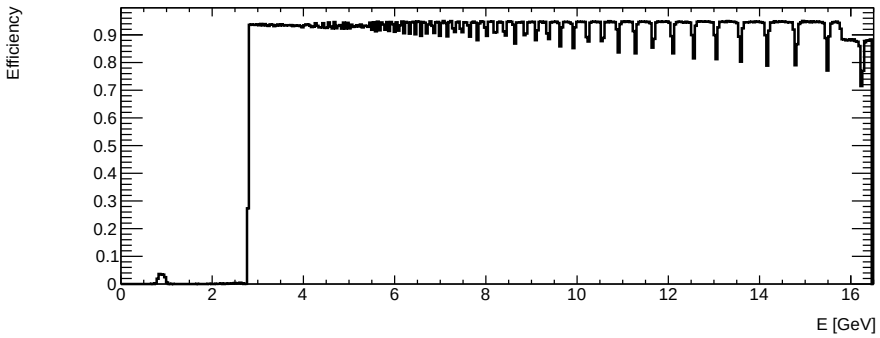

(a)

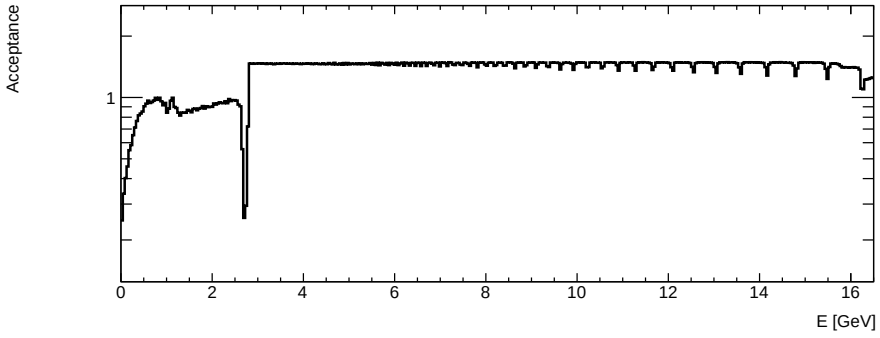

(b)

Figure 13: The detector efficiency (a) and the acceptance (b) as a function of the energy E for the single dense layout.

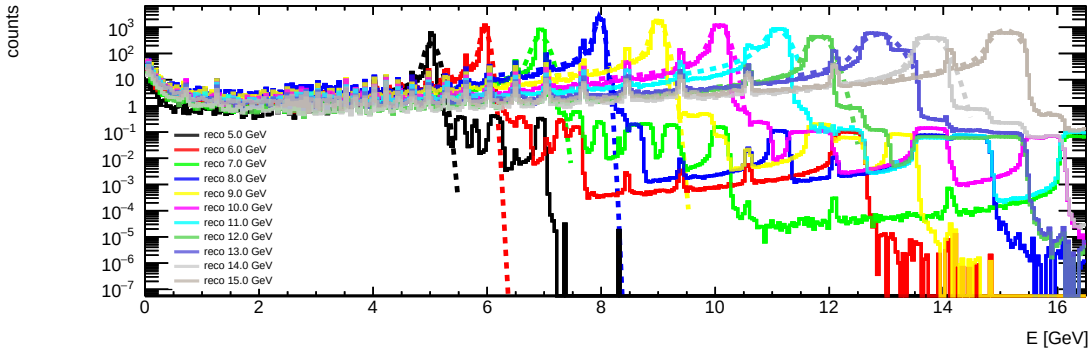

Figure 14: The reconstructed energy distribution for multiple mono-energetic electron samples at energies ranging from $E = 5$ GeV to $E = 15$ GeV with steps of 1 GeV (b). Those results were obtained for the single dense layer layout.

The behaviour of the reconstructed mono-energetic samples is as for the single dense layer layout and the default layout. At energies higher than the main peak, the pattern is now more pronounced, indicating this might be caused by the multiple layers. The

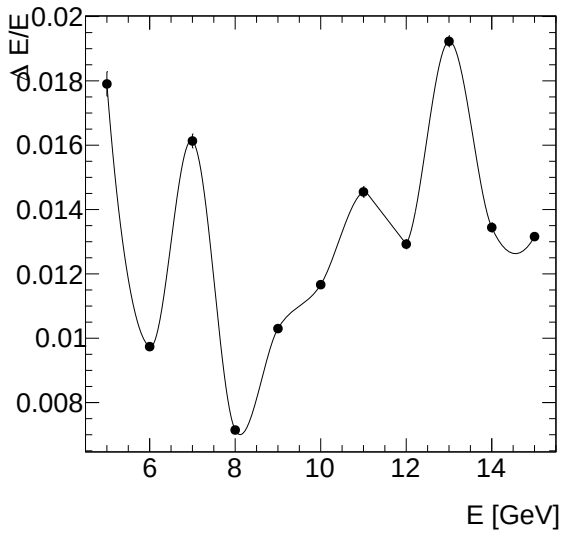

Figure 15: The energy resolution σ_E/E as a function of the energy E for the single dense layer layout.

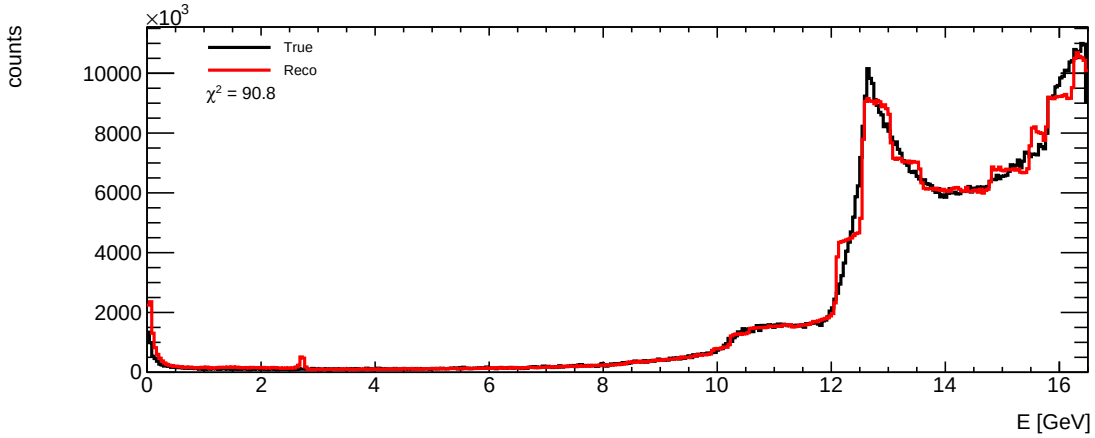

Figure 16: The true and reconstructed energy distributions obtained using the single dense layer layout.

relative energy resolution estimated using the Crystal Ball fits are still showing large fluctuations, but remain under the 2% threshold. The resolution is not improved compared to the single dense layer layout, even though the electrons hit two layers. This results is surprising, as it would have been expected that the more information obtained, the better the resolution.
Finally, the true and reconstructed signal energy distributions are shown on Figure 21. The signal sample is obtained for $\xi = 0.5$. The reconstructed energy distribution is in great agreement with the true distribution, but still shows a bump in the Compton edge.

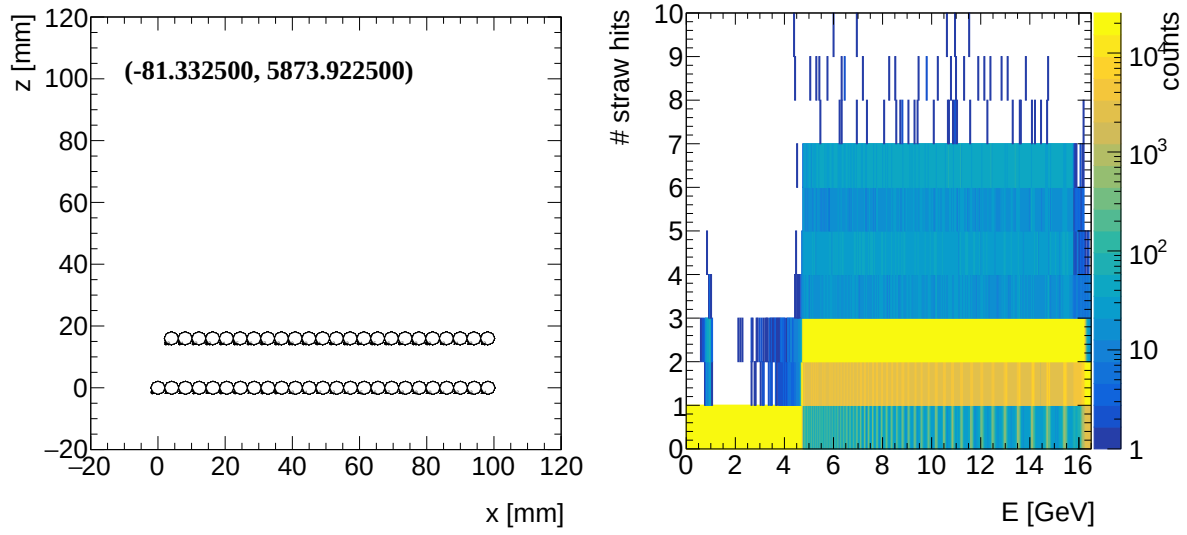

(a) (b)

Figure 17: Detector layout in the xz plane (a) and the number of straw hits per energy E (b) for the double dense layer layout.

4.4. Varied straw sizes

The fourth layout studied is that of a double layer of densely packed straws with varying diameters. The relevant geometric parameters are given in Table 1. A part of the layout is shown in the xz plane on Figure 22a, where the straws continue on the positive x direction in a periodic manner and the axes are centred around the bottom left straw. The number of recorded straw hits per electron energy E is shown on Figure 22b. It was obtained using the flat sample.

The larger straws are not visible on the part of the detector shown on Figure 22a. Still, the lowest detectable energy is 4 GeV, which is lower than that of the double dense layer layout. This is obtained using the same number of straws. Between 4 GeV and 8 GeV, the electrons seem to hit more than two straws. This is surprising, as there are only two layers. Electrons must therefore enter the detector with such an angle as to pass through two straws of the same layer. Above 8 GeV, the behaviour is exactly the same as for the double dense layers layout.

The efficiency of the Cerenkov detector as a function of the electron energy E is shown on Figure 23a, using the flat sample. The energy acceptance as a function of the energy E is presented on Figure 23b using a log vertical scale; it was obtained using the flat sample.

The efficiency as a function of the energy shows the lowered detection limit as well, whilst the acceptance shows the complications created by the multiple straw hits between 4 GeV and 8 GeV. The drop in acceptance at around 4 GeV is an artefact caused by the reconstruction method; the effect coincides with the end of the Cerenkov box.

The reconstructed energy distribution and their Crystal Ball fit for multiple separate

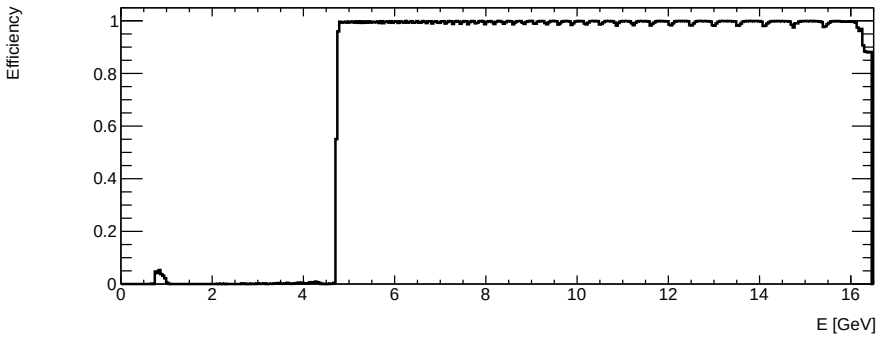

(a)

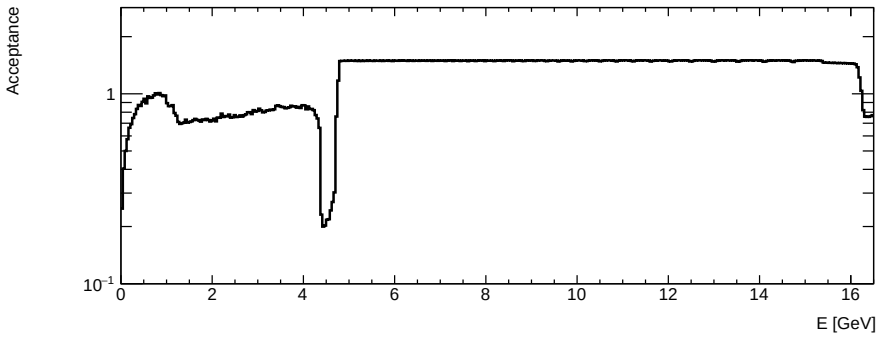

(b)

Figure 18: The detector efficiency (a) and the acceptance (b) as a function of the energy E for the double dense layout.

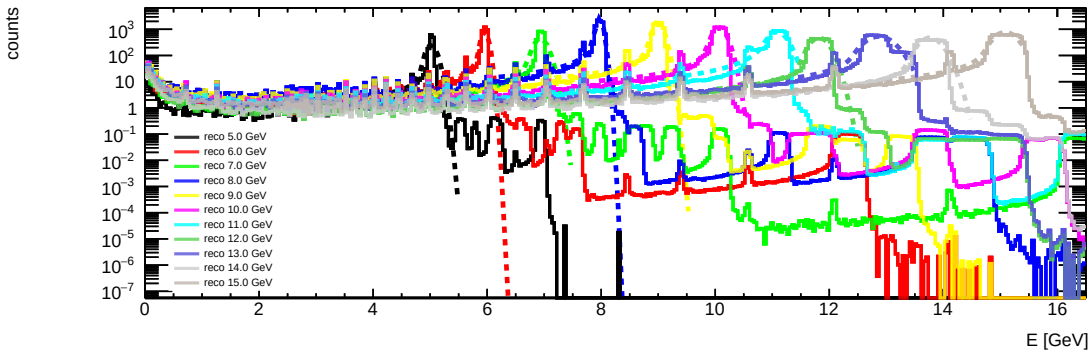

Figure 19: The reconstructed energy distribution for multiple mono-energetic electron samples at energies ranging from $E = 5$ GeV to $E = 15$ GeV with steps of 1 GeV (b). Those results were obtained for the double dense layer layout.

mono-energetic electron samples are shown on Figure 24. The energies of the samples cover the range from 5 GeV to 15 GeV in steps of 1 GeV. The reconstructed mono-energetic shows the same general behaviour as the double dense layer layout. There are

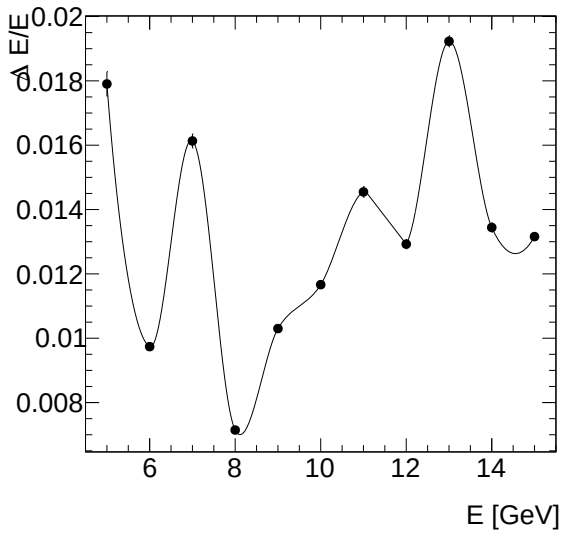

Figure 20: The energy resolution σ_E/E as a function of the energy E for the double dense layer layout.

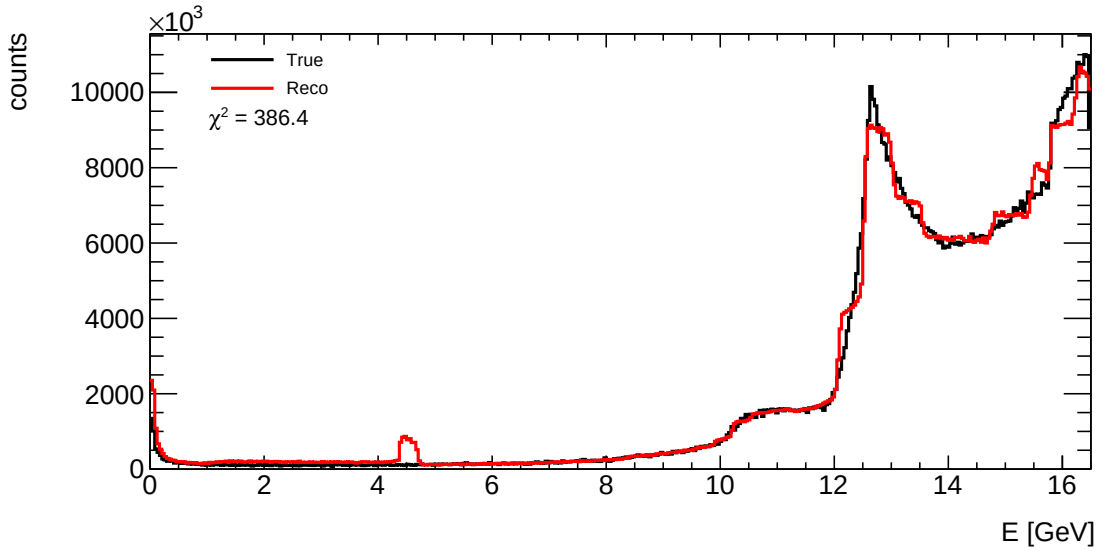

Figure 21: The true and reconstructed energy distributions obtained using the double dense layer layout.

however more bumps at energies above the main peak. Furthermore, the mono-energetic sample at $E = 11$ GeV shows two steps in the main peak. This can be caused by the fact that the electrons at this energy are detected in the interface between the smaller and larger straws. Therefore, electrons hitting the last (right-most) small straw of the first layer can hit the first (left-most) large straw of the second layer.
The energy resolution σ_E/E estimated using the fits is shown as a function of the electron

energy E on Figure 25. Finally, the true and reconstructed signal energy distributions are shown on Figure 26. The signal sample is obtained for $\xi = 0.5$. As for the other layouts, the relative energy resolution σ_E/E remains smaller than the threshold value, even though there are large fluctuations. The reconstructed energy distribution remains in great agreement with the true distribution. The reconstructed Compton edge does not show a bump as large as for the double dense layer layout, but the wiggly behaviour for energies larger than the that of the edge is a strong as before. A small peak at 4 GeV is visible and is most likely caused by the sudden drop in acceptance.

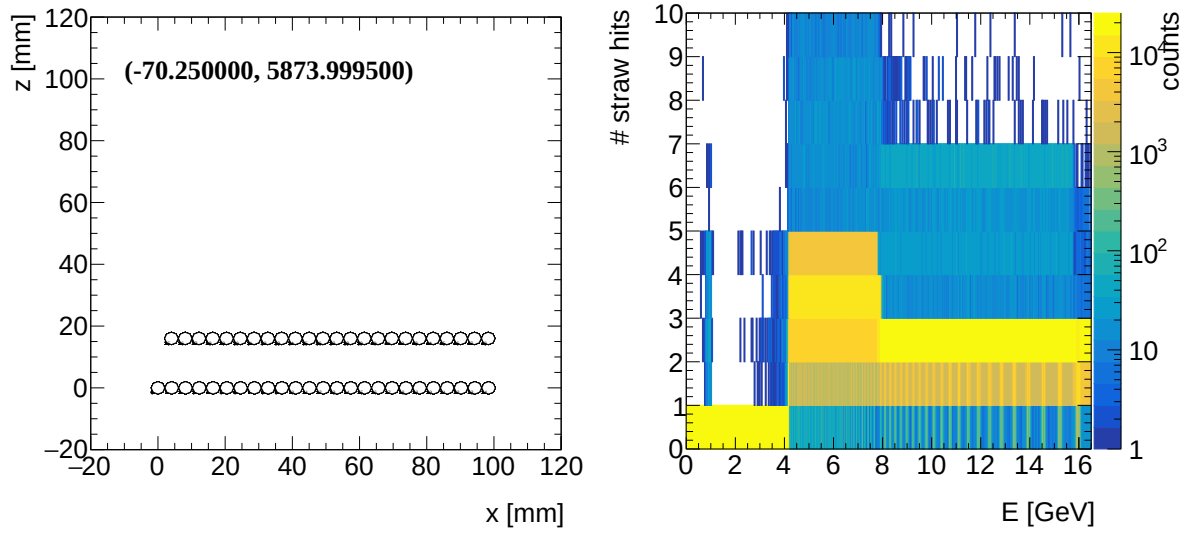

(a) (b)

Figure 22: Detector layout in the xz plane (a) and the number of straw hits per energy E (b) for the varied straw sizes layout.

4.5. Heavily tilted layers

The fourth layout studied is that of a double layer of densely packed straws with varying diameters. The relevant geometric parameters are given in Table 1. A part of the layout is shown in the xz plane on Figure 27a, where the straws continue on the positive x direction in a periodic manner and the axes are centred around the bottom left straw. The number of recorded straw hits per electron energy E is shown on Figure 27b. It was obtained using the flat sample.

The heavily tilted layout presented in Figure 27a has been chosen such that the only way for an electron to go through the detector without hitting any straw requires an entry angle lower than the entry angle of the lowest energy electrons of interest. This is confirmed by the result shown on Figure 27b; neglecting the electrons with energies too low to be detected ($E < 3$ GeV), most electrons have at least one hit. The majority show two hits. Only the highest energy electrons ($E > 15$ GeV) have only one hit, because

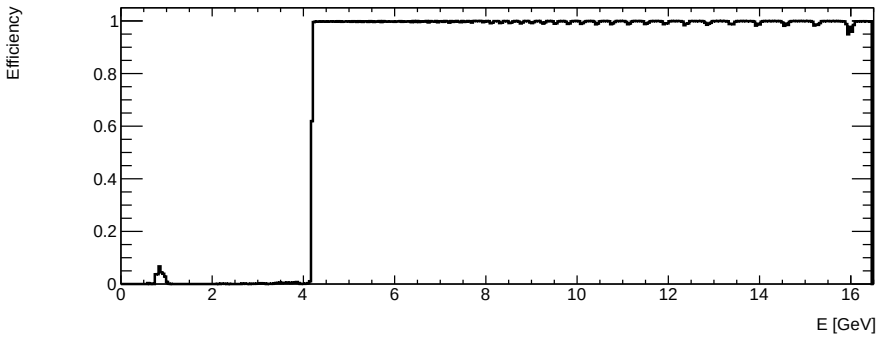

(a)

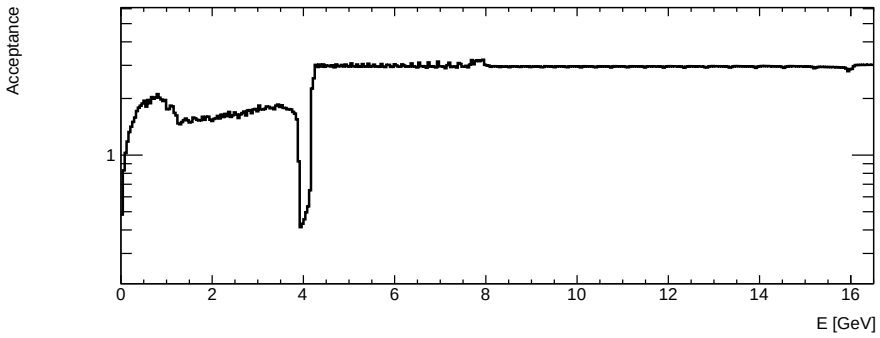

(b)

Figure 23: The detector efficiency (a) and the acceptance (b) as a function of the energy E for the varied straw sizes layout.

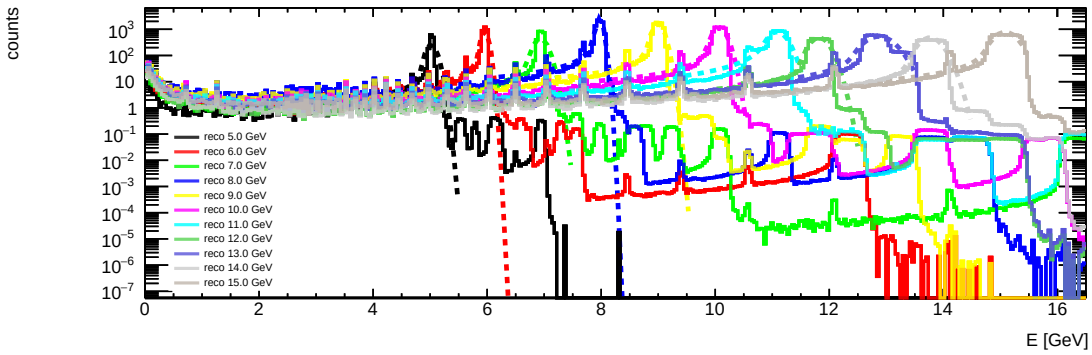

Figure 24: The reconstructed energy distribution for multiple mono-energetic electron samples at energies ranging from $E = 5$ GeV to $E = 15$ GeV with steps of 1 GeV (b). Those results were obtained for the varied straw sizes layout.

their entry angle is shallow enough that they do no hit the first (left-most) straw of the second layer. If multiple hits was a requirement, this shortcoming could easily be fixed by adding a special straw. It could be set on the third layer, with its centre x position

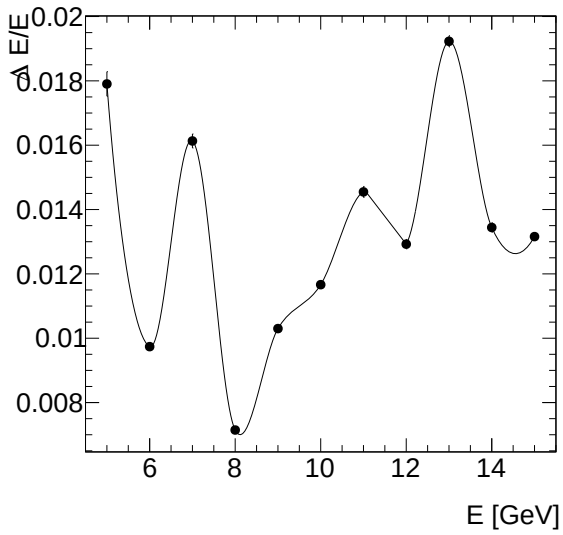

Figure 25: The energy resolution σ_E/E as a function of the energy E for the varied straw sizes layout.

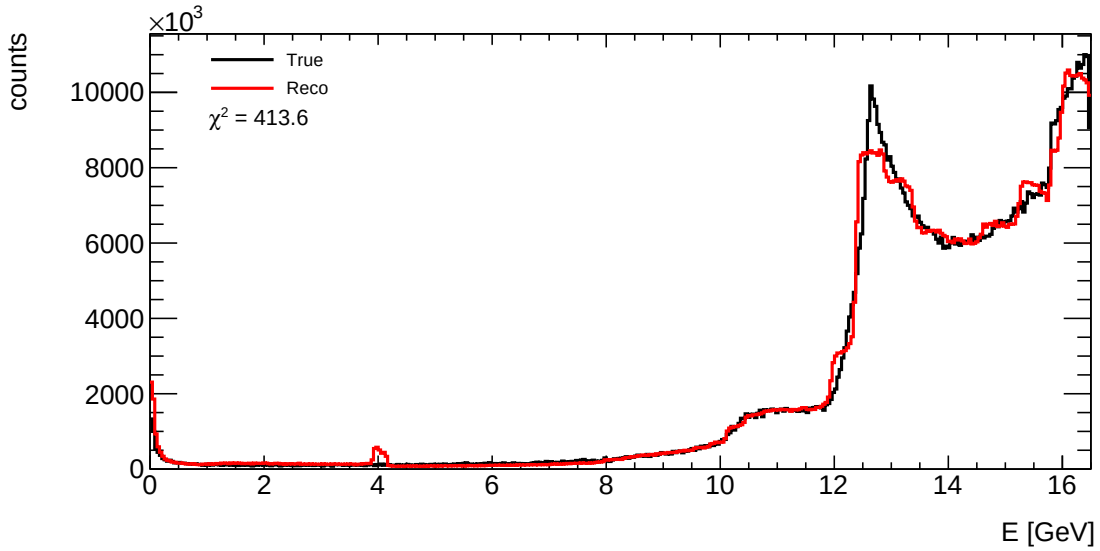

Figure 26: The true and reconstructed energy distributions obtained using the varied straw sizes layout.

in between that of the left-most straw of the first and third layers. The heavily tilted layout would make such an addition easier than for other layouts.
The same information can be gathered from the efficiency as a function of the electron energy E shown on Figure 28a; this result was obtained using the flat sample. In particular, the drop-off at high energies is more pronounced than for the other layouts; this is expected because they do not have such a large offset from layer to layer. The

energy acceptance as a function of the energy E is presented on Figure 28b using a log vertical scale; it was obtained using the flat sample.
The reconstructed energy distribution and their Crystal Ball fit for multiple separate mono-energetic electron samples are shown on Figure 29. The energies of the samples cover the range from 5 GeV to 15 GeV in steps of 1 GeV. The energy resolution σ_E/E estimated using the fits is shown as a function of the electron energy E on Figure 30. Finally, the true and reconstructed signal energy distributions are shown on Figure 31. The signal sample is obtained for $\xi = 0.5$.
The reconstructed mono-energetic samples show the same behaviour as the other layouts. Therefore it is not unexpected that the relative energy resolution remains under the 2% threshold while showing large fluctuations. The energy distribution reconstruction is similar to that obtained using other layouts. There is a more important bump in the reconstructed Compton edge compared to the layout with varied straw sizes. The reconstruction matches closely the true distribution nonetheless.

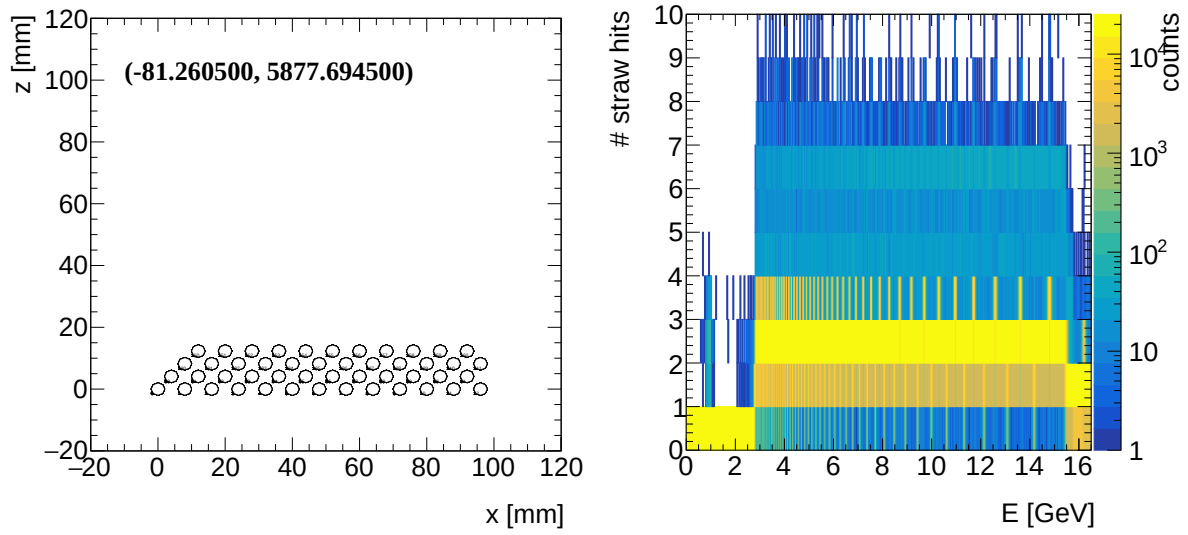

(a) (b)

Figure 27: Detector layout in the xz plane (a) and the number of straw hits per energy E (b) for the heavily tilted layout.

5. Future work

For the construction of the transfer matrix, one important step is the matching between straw hits and virtual front plane hits. In this study, the matching has been done by finding the smallest distance between the extrapolated front plane hit and the recorded front plane hits. The extrapolation was done using the position of the straw hits. This technique is not guaranteed to work for events where electrons were scattered before

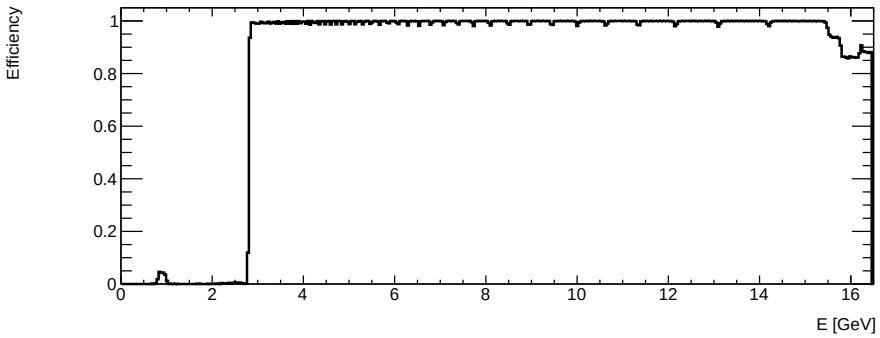

(a)

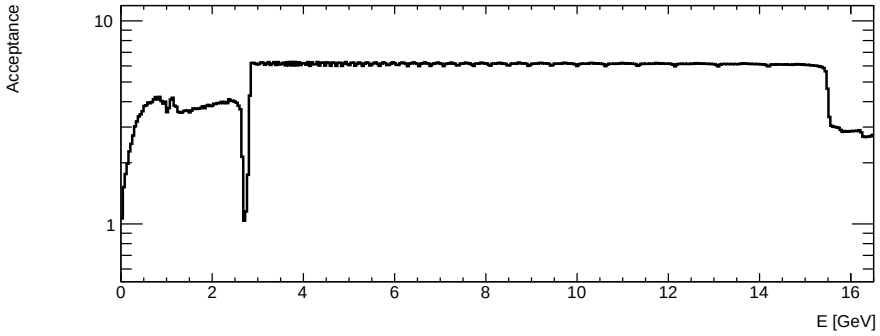

(b)

Figure 28: The detector efficiency (a) and the acceptance (b) as a function of the energy E for the heavily tilted layout.

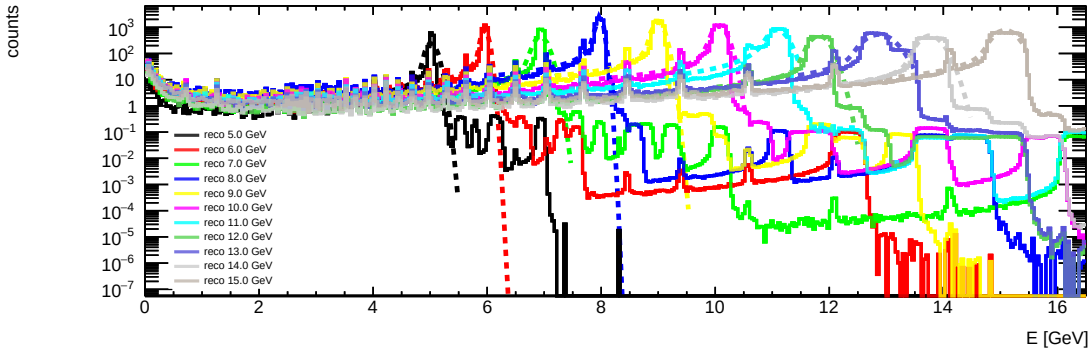

Figure 29: The reconstructed energy distribution for multiple mono-energetic electron samples at energies ranging from $E = 5$ GeV to $E = 15$ GeV with steps of 1 GeV (b). Those results were obtained for the heavily tilted layout.

entering the box and as well inside of the Cerenkov box. In that case, multiple hits will be recorded on the virtual front plane and the angles at which the electrons scattered inside the box can lead to false matching. The error rate in the matching should be

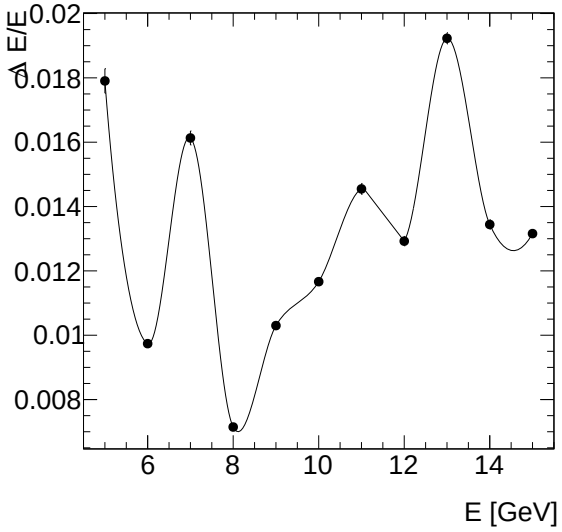

Figure 30: The energy resolution σ_E/E as a function of the energy E for the heavily tilted layout.

studied further, and an improved method should be considered if necessary.
The choice of a Crystal ball function to fit is justified by the lower tail present in the reconstructed mono-energetic samples and the general good agreement between fit and data. Nonetheless, this function does not reproduce the proper shape of the main peaks at higher energies. Indeed, the peaks are flatter, more square, than a Gaussian peak. This means the actual energy resolution would be slightly larger than that extracted using the Gaussian standard deviation σ_E. More importantly, the reconstruction introduces secondary peaks when the efficiency drops. This increases noise in other energy ranges, which will then reduce the energy resolution at those energies. The fact that the whole path length distribution is transformed into the whole energy distribution means that those effects can play a role. Therefore, studying the energy resolution at separate energies is limited.
Also, the path length is know perfectly in this study. This will not the case when LUXE will be taking measurements, as the photo detectors have a finite precision. Therefore, this uncertainty will be carried on in the reconstruction. This increases the uncertainty on the reconstructed energy distribution. Such effect should be taken into account when studying the energy resolution.
This preliminary study does not take into account background noise caused by the scattering of electrons on the different elements. In particular, the reduced LUXE Geant4 simulation used does not model the beam dump. This is expected to reduce the energy resolution.
Furthermore, the impact imperfections in the physical Cerenkov detector should also be studied further. Indeed, a detector design is tolerant for a faulty component. A single layer design would, for instance, be strongly impacted by a malfunctioning straw. Furthermore, the position of the straw can only be guaranteed to some finite precision,

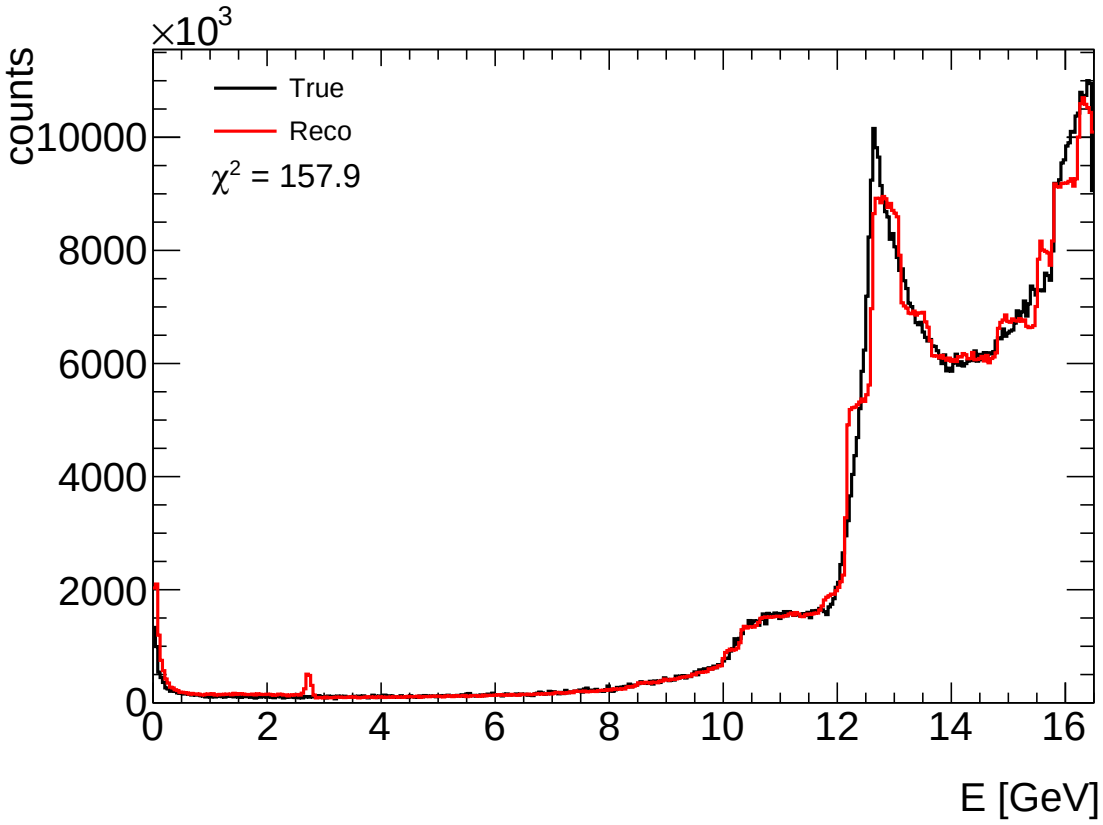

Figure 31: The true and reconstructed energy distributions obtained using the heavily tilted layout.

meaning that small shifts in position should also be taken into account. Both of these considerations would be arguments for a design containing multiple layers.

6. Conclusion

This study has shown that the energy distribution can be reconstructed accurately despite the high electron rate. The effects on the measurements of the different parameters defining the Cerenkov detector layout have been explored. Furthermore, a first estimate of the energy resolution has been put together. The results suggest that the reconstruction method and the layouts proposed in this study would be sufficient to measure the effects with the required precision. Multiple layouts satisfying the requirements defined at the beginning have been found; the open options would allow for more stringent requirements.

Importantly, this study has lead to further considerations. Alternative reconstruction methods should be considered to extract more information. The independent measurements of the different straws could be used for pattern matching using machine learning between path length in the straws and energy distribution. As for the energy resolution,

a systematic error study should be performed. Such work would provide a more precise understanding of the errors and would be expected to highlight a layout dependence that has not been found.

References

[1] Geant4—a simulation toolkit, S.Agostinelli et al., Nuclear Instruments and Methods in Physics Research Section A: Accelerators, Spectrometers, Detectors and Associated Equipment, Volume 506, Issue 3, 1 July 2003, Pages 250-303

[2] Executive Summary and Physics Prospects, LUXE Collaboration, 27.03.2022

[3] Conceptual design report for the LUXE experiment, LUXE Collaboration, September 2022

[4] Calculation of the Cherenkov Light Yield for High-Energy Particle Cascades, Omer Penek, Fakultät für Mathematik, Informatik und Naturwissenschaften der RWTH Aachen, 02.05.2016

[5] Frank-Tamm formula, wikipedia, visited on 07.09.2022
https://en.wikipedia.org/wiki/Frank-Tamm_formula

[6] Ptarmigan generator, Tom G. Blackburn,
https://github.com/tgblackburn/ptarmigan

[7] Crystal Ball function, Wikipedia, visited on 05.09.2022
https://en.wikipedia.org/wiki/Crystal_Ball_function

A. Additional layout results

Some additional layouts are presented in the following chapters. The parameters defining the geometry are given in Table 2.

	Channels	Layers	Diameter	x frequency	z frequency	Offset
Four dense	200	4	4.02 mm	4.02 mm	16 mm	4 mm
Larger straws	100	2	6 mm	6.1 mm	16 mm	4 mm
Aluminium	100	1	4.02 mm	6.1 mm	16 mm	4 mm

Table 2: Geometric parameters of the Cerenkov straw detector in the additional layouts.

A.1. Four dense layers

The first additional layout studied is that of four layers of densely packed straws. The relevant geometric parameters are given in Table 2. A part of the layout is shown in the xz plane on Figure 32a, where the straws continue on the positive x direction in a periodic manner and the axes are centred around the bottom left straw. The number of recorded straw hits per electron energy E is shown on Figure 32b. It was obtained using the flat sample. The efficiency of the Cerenkov detector as a function of the electron energy E is shown on Figure 33a, using the flat sample. The energy acceptance as a function of the energy E is presented on Figure 33b using a log vertical scale; it was obtained using the flat sample. The reconstructed energy distribution and their Crystal Ball fit for multiple separate mono-energetic electron samples are shown on Figure 34. The energies of the samples cover the range from 5 GeV to 15 GeV in steps of 1 GeV. The energy resolution σ_E/E estimated using the fits is shown as a function of the electron energy E on Figure 35. Finally, the true and reconstructed signal energy distributions are shown on Figure 36. The signal sample is obtained for $\xi = 0.5$.

A.2. Larger straws

The second additional layout studied is that of a double layer of densely packed straws with a larger straw diameters of 6 mm. The relevant geometric parameters are given in Table 2. A part of the layout is shown in the xz plane on Figure 37a, where the straws continue on the positive x direction in a periodic manner and the axes are centred around the bottom left straw. The number of recorded straw hits per electron energy E is shown on Figure 37b. It was obtained using the flat sample. The efficiency of the Cerenkov detector as a function of the electron energy E is shown on Figure 38a, using the flat sample. The energy acceptance as a function of the energy E is presented on Figure 38b using a log vertical scale; it was obtained using the flat sample. The reconstructed energy distribution and their Crystal Ball fit for multiple separate mono-energetic electron samples are shown on Figure 39. The energies of the samples cover the range from 5 GeV to 15 GeV in steps of 1 GeV. The energy resolution σ_E/E estimated

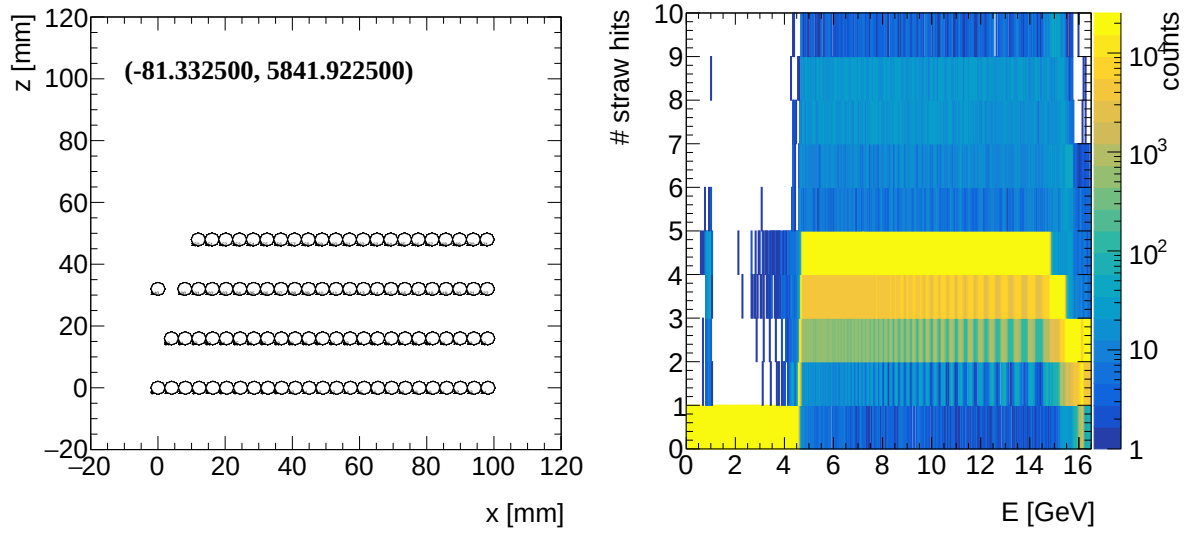

(a) (b)

Figure 32: Detector layout in the xz plane (a) and the number of straw hits per energy E (b) for the four dense layers layout.

using the fits is shown as a function of the electron energy E on Figure 40. Finally, the true and reconstructed signal energy distributions are shown on Figure 41. The signal sample is obtained for $\xi = 0.5$.

A.3. Aluminium straws

The third additional layout studied is that of a single layer of densely packed straws made of aluminium. The relevant geometric parameters are given in Table 2. A part of the layout is shown in the xz plane on Figure 42a, where the straws continue on the positive x direction in a periodic manner and the axes are centred around the bottom left straw. The number of recorded straw hits per electron energy E is shown on Figure 42b. It was obtained using the flat sample. The efficiency of the Cerenkov detector as a function of the electron energy E is shown on Figure 43a, using the flat sample. The energy acceptance as a function of the energy E is presented on Figure 43b using a log vertical scale; it was obtained using the flat sample. The reconstructed energy distribution and their Crystal Ball fit for multiple separate mono-energetic electron samples are shown on Figure 44. The energies of the samples cover the range from 5 GeV to 15 GeV in steps of 1 GeV. The energy resolution σ_E/E estimated using the fits is shown as a function of the electron energy E on Figure 45. Finally, the true and reconstructed signal energy distributions are shown on Figure 46. The signal sample is obtained for $\xi = 0.5$.

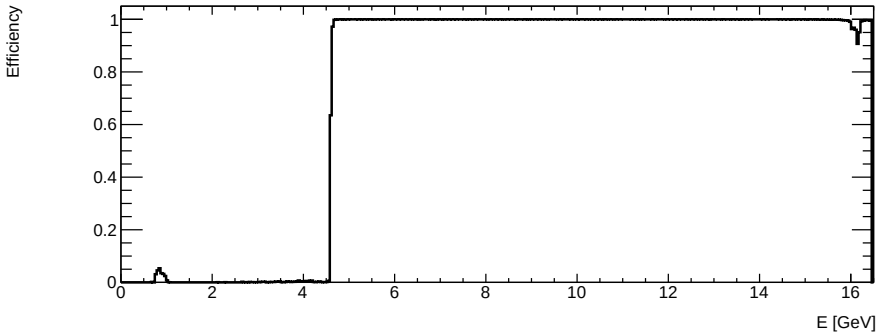

(a)

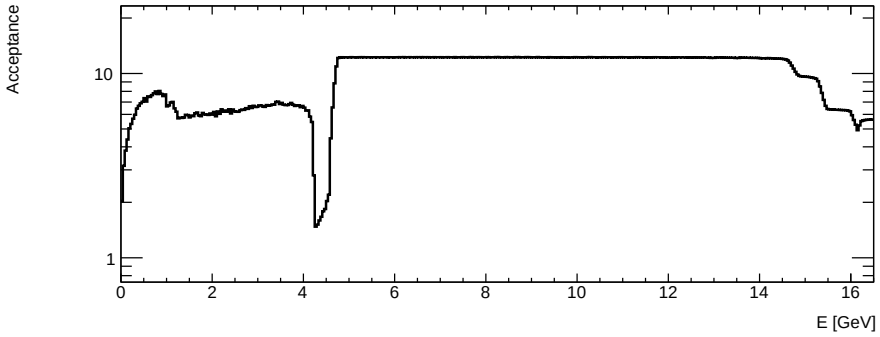

(b)

Figure 33: The detector efficiency (a) and the acceptance (b) as a function of the energy E for the four dense layers layout.

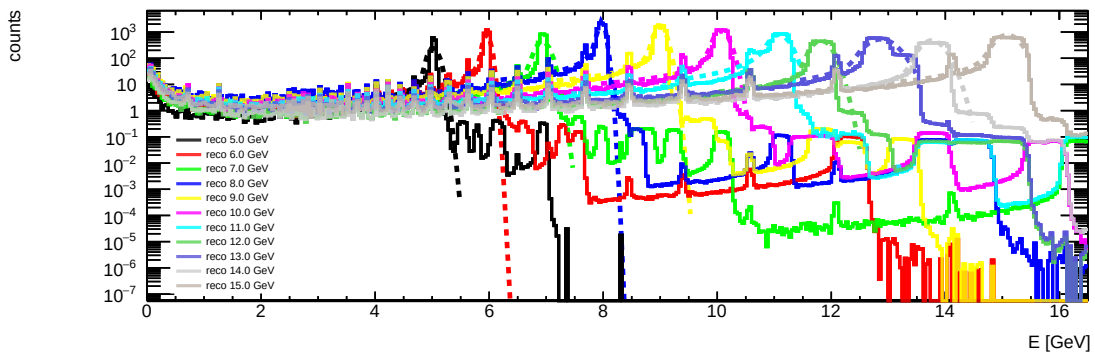

Figure 34: The reconstructed energy distribution for multiple mono-energetic electron samples at energies ranging from $E = 5$ GeV to $E = 15$ GeV with steps of 1 GeV (b). Those results were obtained for the four dense layers layout.

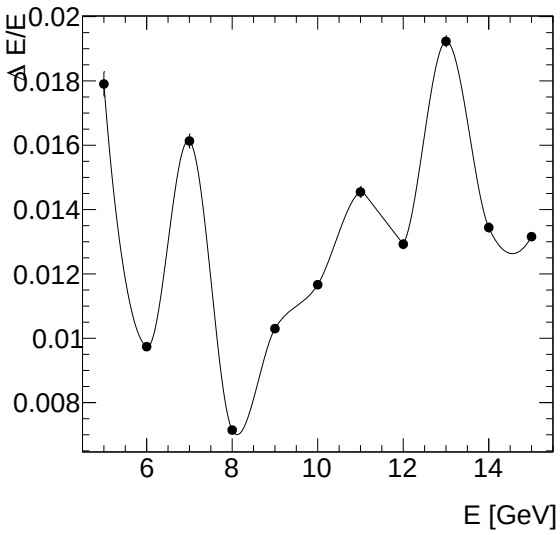

Figure 35: The energy resolution σ_E/E as a function of the energy E for the four dense layers layout.

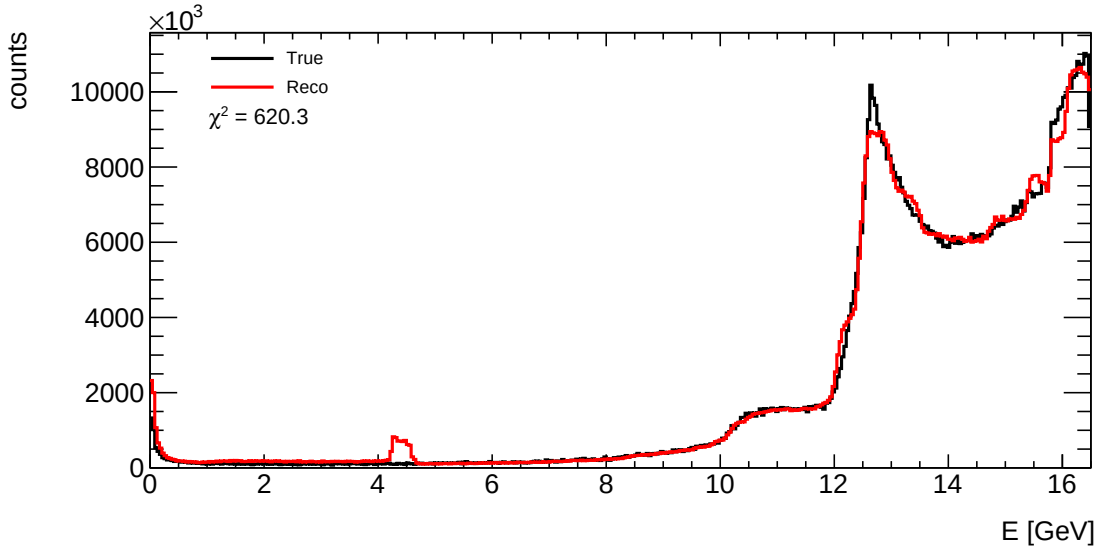

Figure 36: The true and reconstructed energy distributions obtained using the four dense layers layout.

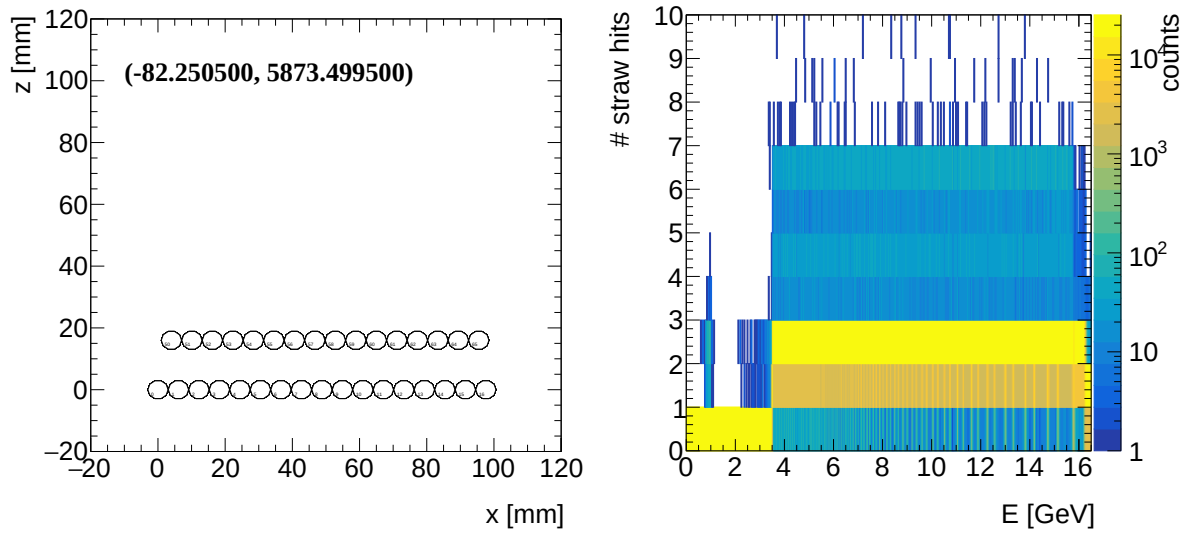

(a) (b)

Figure 37: Detector layout in the xz plane (a) and the number of straw hits per energy E (b) for the larger straw diameter layout.

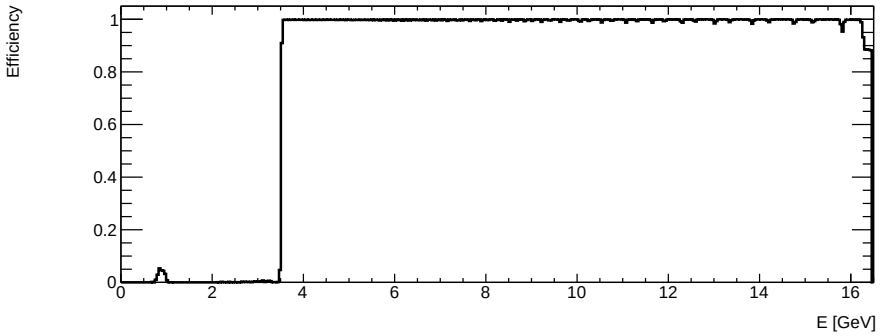

(a)

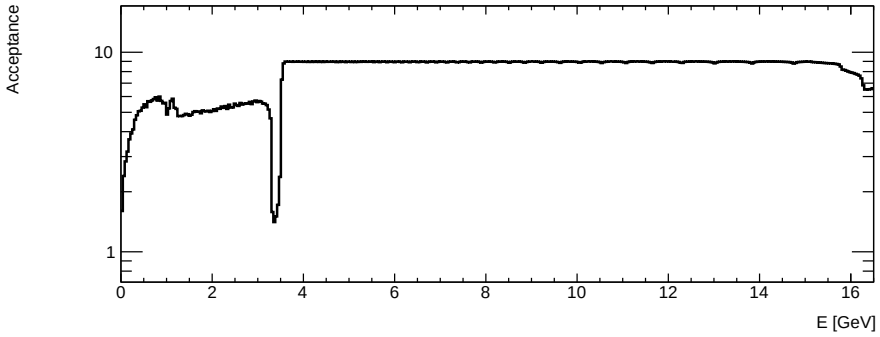

(b)

Figure 38: The detector efficiency (a) and the acceptance (b) as a function of the energy E for the larger straw diameter layout.

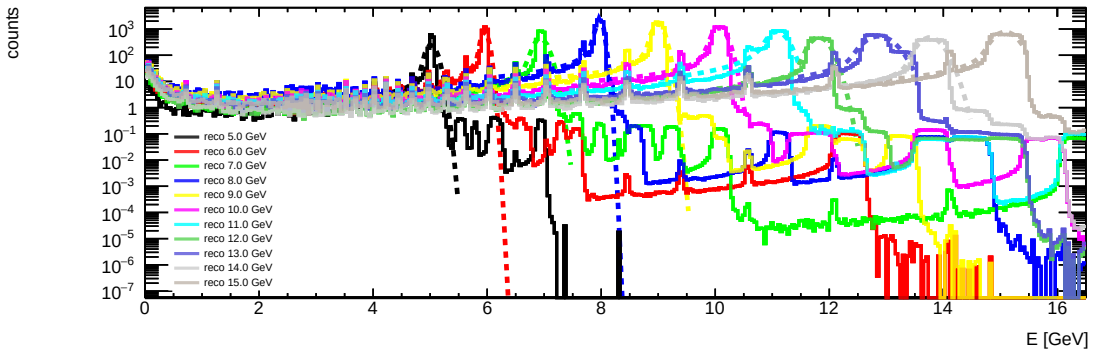

Figure 39: The reconstructed energy distribution for multiple mono-energetic electron samples at energies ranging from $E = 5$ GeV to $E = 15$ GeV with steps of 1 GeV (b). Those results were obtained for the larger straw diameter layout.

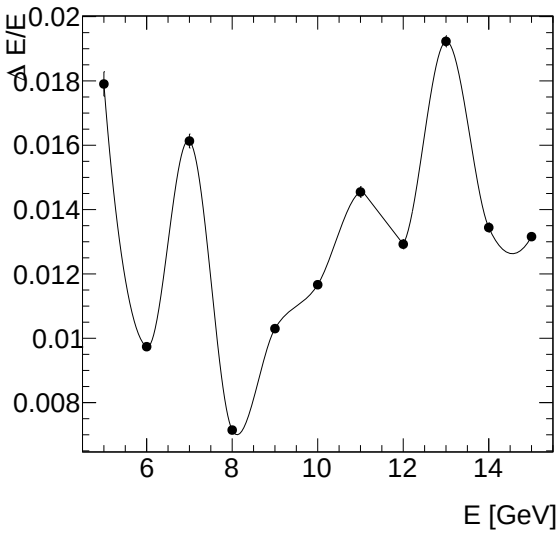

Figure 40: The energy resolution σ_E/E as a function of the energy E for the larger straw diameter layout.

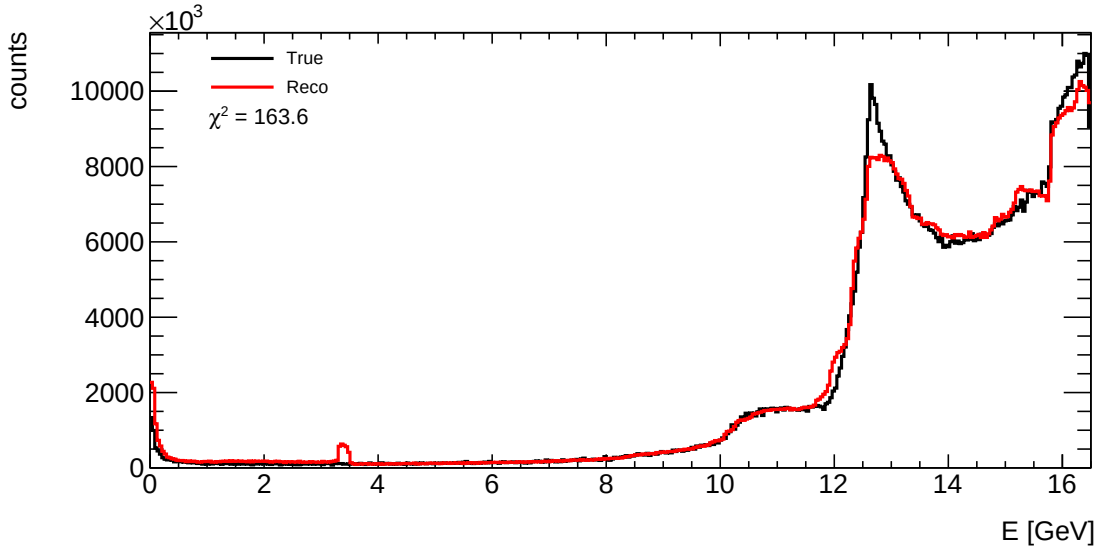

Figure 41: The true and reconstructed energy distributions obtained using the larger straw diameter layout.

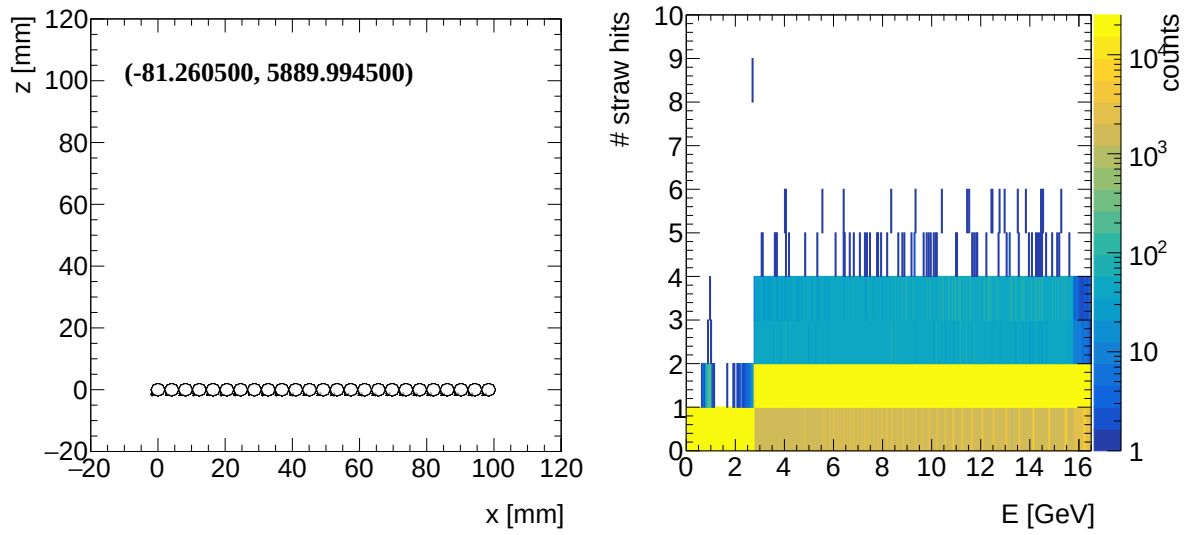

(a) (b)

Figure 42: Detector layout in the xz plane (a) and the number of straw hits per energy E (b) for the aluminium straw layout.

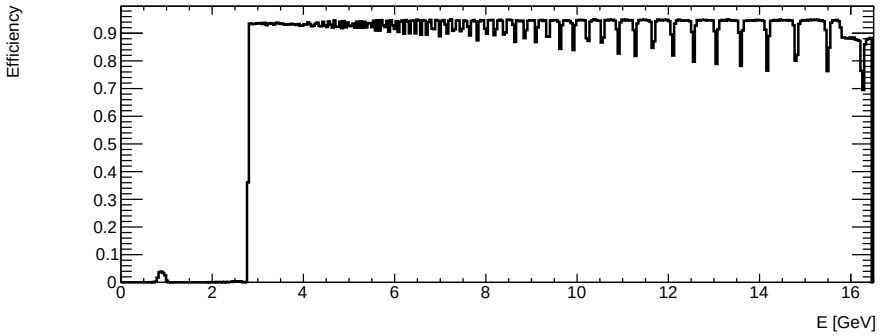

(a)

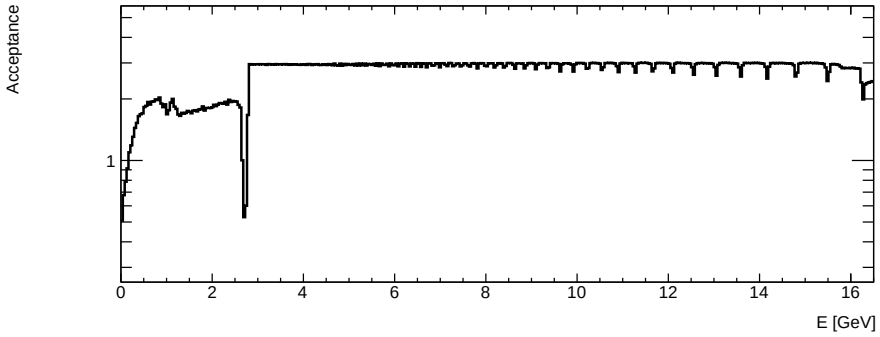

(b)

Figure 43: The detector efficiency (a) and the acceptance (b) as a function of the energy E for the aluminium straw layout.

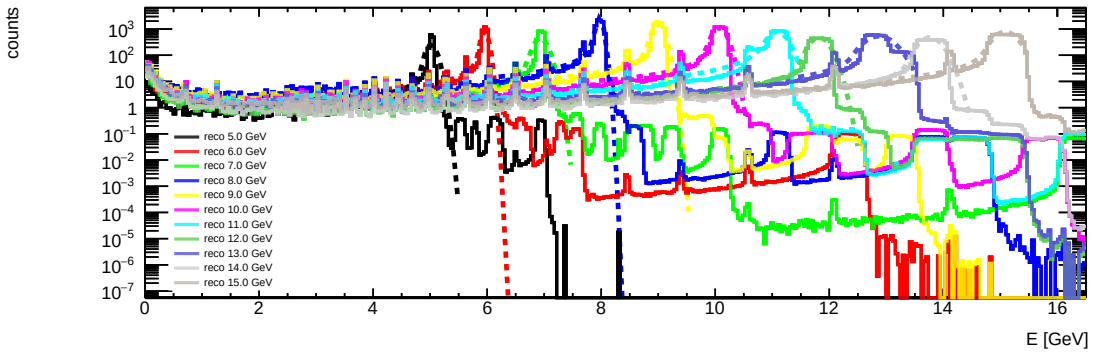

Figure 44: The reconstructed energy distribution for multiple mono-energetic electron samples at energies ranging from $E = 5$ GeV to $E = 15$ GeV with steps of 1 GeV (b). Those results were obtained for the aluminium straw layout.

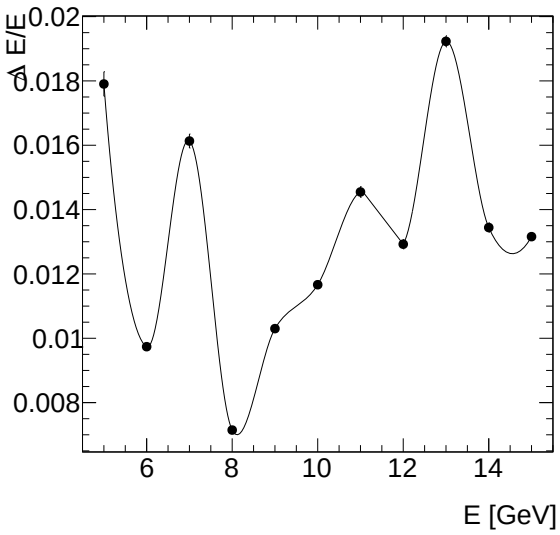

Figure 45: The energy resolution σ_E/E as a function of the energy E for the aluminium straw layout.

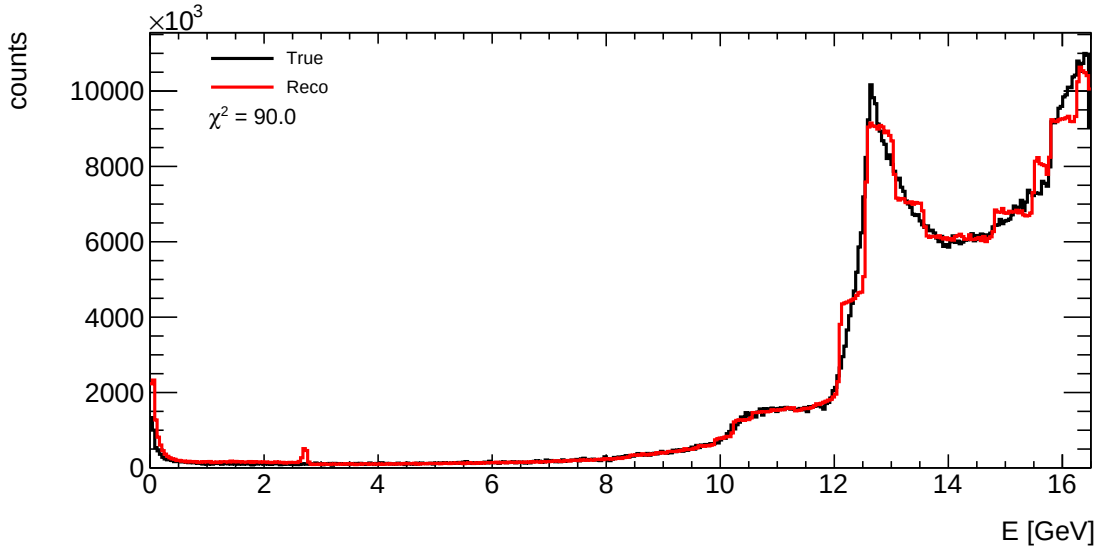

Figure 46: The true and reconstructed energy distributions obtained using the aluminium straw layout.